Helsinki University of Technology
Laboratory of Computational Engineering
Espoo 2004

REPORT B41

MOLECULAR DYNAMICS SIMULATIONS OF STRAINED AND DEFECTIVE CARBON NANOTUBES

Maria Sammalkorpi

Dissertation for the degree of Doctor of Science in Technology to be presented with due permission of the Department of Electrical and Communications Engineering, Helsinki University of Technology, for public examination and debate in Auditorium T2 at Helsinki University of Technology (Espoo, Finland) on the 17th of December, 2004, at 12 noon.

Helsinki University of Technology
Department of Electrical and Communications Engineering
Laboratory of Computational Engineering

Teknillinen korkeakoulu
Sähkö- ja tietoliikennetekniikan osasto
Laskennallisen tekniikan laboratorio

Abstract

Carbon nanotubes are tubular molecules of pure carbon with typical diameters of 1 nm – 100 nm and lengths from 100 nm up to several cm. The nanotubes have outstanding electronical and mechanical properties which has resulted in remarkable scientific interest and in proporsals of various applications. For example, their ability to be either metals or semiconductors enables the usage of nanotubes as components of electronic devices, while excellent mechanical characteristics motivate the use of nanotubes as reinforcement agents in composite structures and in nanoelectromechanical devices.

This thesis aims to contribute to the understanding of the mechanical properties of carbon nanotubes and it contains two parts. The first part concentrates on initially defect-free but strained nanotubes and on the deformations and defects induced by the strain. The employed methods are empirical and tight binding molecular dynamics simulations. As results the criteria for uniform and discontinuous buckling deformations are reported. In addition, defect formation and strain relaxation are discussed and the stability of various strained and deformed structures is assessed.

The second part of the thesis evaluates defects as a means to improve the bulk mechanical properties of a nanotube sample. Defects, and irradiation as a method of inducing them, are proposed to improve mechanical load transfer between a nanotube and its surroundings. These proposals are verified by analytics and molecular dynamics simulations based on classical empirical potential. The load transfer between nanotubes is found to improve significantly in the presence of defects. This concept is extended to bundles of nanotubes where the improved tube-tube load transfer is predicted to increase shear and stiffen the bundle at moderate irradiation doses. The load transfer has great significance for reinforcement of polymer composites in which the nanotube bundles may act as reinforcement fibers. Furthermore, the mechanical degradation of individual tubes as a result of the defects is also assessed. Point defects have little effect on the axial stiffness of an individual tube but the tensile strength may decrease to a fraction of the strength for a perfect tube. Although individual tubes deteriorate in strength because of the defects, the results indicate that the overall mechanical properties of a nanotube sample can be significantly improved by imperfections

in the structure of the tubes.

Preface

This thesis is the result of research work performed during the years 2001-2004 at Laboratory of Computational Engineering, Helsinki University of Technology. This has been a fascinating and delightful time of learning but, like most theses, also this one has caused moments of anxiety, frustration and even desperation. There are several people who smoothened the way. First of all, I want to thank Dr. Arkady Krasheninnikov who raised the questions, and taught how to answer them. My supervisor Prof. Kimmo Kaski provided excellent facilities and environment for this study. He never lacked in supporting words and encouragement. Dr. Antti Kuronen was there always to help. I am also grateful to Prof. Kai Nordlund for the opportunity to collaborate with him and his group. Jussi Aittoniemi and Kaisa Kautto: It has been a pleasure to work side-by-side with such smart and diligent people. I wish we could have had more time together. Dr. Michael Patra deserves my gratitude for the physics insight and the computer environment tricks and treats that went way beyond his post.

Besides colleagues, I have been lucky to have plenty of peer support in this project. Dear friends, fellow doctoral students in various fields, many thanks for letting me share the good and the bad moments. It has really made a difference. I owe much to my parents Maritta and Markku for they have never shown anything but support and belief in me, and to my sister Elina for all the moments we have shared. Finally, this thesis may well not have seen the daylight were it not for my husband Ville who has a hearty embrace, remarkable skill of posing the right questions and who, despite what he may claim, has never ceased to be a physicist at heart.

Maria Sammalkorpi

List of publications

This dissertation consists of an overview and the following publications:

I. M. Huhtala, A. Kuronen, K. Kaski, *Carbon nanotube structures: molecular dynamics at realistic limit*, Computer Physics Communications **146**, 30 (2002).

II. M. Huhtala, A. Kuronen, K. Kaski, *Computational Studies of Carbon Nanotube Structures*, Computer Physics Communications **147**, 91 (2002).

III. M. Huhtala, A. Kuronen, K. Kaski, *Carbon nanotubes under bending strain*, in Making Functional Materials with Nanotubes, volume **706** of Materials Research Society Symposium Proceedings, Eds. P. Bernier, P. Ajayan, Y. Iwasa, P. Nikolaev, pp. 289, Materials Research Society, 2002.

IV. M. Huhtala, A. V. Krasheninnikov, J. Aittoniemi, S. J. Stuart, K. Nordlund, K. Kaski, *Improved mechanical load transfer between shells of multi-walled carbon nanotubes*, Physical Review B **70**, 045404 (2004).

V. M. Sammalkorpi, A. V. Krasheninnikov, A. Kuronen, K. Nordlund, K. Kaski, *Mechanical properties of carbon nanotubes with vacancies and related defects*, accepted for publication in Phys. Rev. B (2004).

VI. M. Sammalkorpi, A. V. Krasheninnikov, A. Kuronen, K. Nordlund, K. Kaski, *Irradiation-induced stiffening of carbon nanotube bundles*, accepted for publication in Nucl. Instr. and Meth. in Phys. B (2004).

In the overview these publications are referred to by their roman numerals.

The author Maria Sammalkorpi (née Huhtala) has had an active role in all stages of the research reported in this thesis. She has designed and implemented the computer program employed in Publications I-III. She is responsible for planning and conducting all the simulations in Publications I-III, V and VI, and most of the simulations in Publication IV. The author has participated in the theoretical formulation of Publications IV and V and done the theory formulation of Publication VI. She has done the data analysis and written all the publications under the supervision and guidance of senior scientists.

Contents

Chapter 1

Introduction

Carbon is a very special element: Its electronic structure is $1s^2 2s^2 2p^2$ and the $2s$ electrons readily participate in molecular bonding. This enables a wide variety of bonding configurations and allotropes as different as the ultra-hard, brittle and insulating diamond and layer-wise lubricant semimetal graphite. More recently an even wider set of properties has been discovered with various carbon nano-structures such as fullerenes, diamondoids, nano-onions and carbon nanotubes. Although the nanostructures have opened new possibilities in the electronics, the traditional uses for carbon are mechanical in nature. Examples of this are the hard synthesized diamond and diamond coatings, the carbon fibers and whiskers in reinforcement of composite structures, and the smooth graphite in lubrication and surface processes.

In this thesis the focus is on novel carbon nanostructures, more specifically on carbon nanotubes. The history of carbon nanotubes dates back to the question of smallest possible carbon fiber in the 1970's when ultra-thin carbon fibers were synthesized. Despite the fullerene initiated [1] incentive on carbon nanostructures, it was by chance that Sumio Iijima took interest in the carbon soot he had and made his interpretation: tiny concentric shells of graphene in the form of mini-ature tubules [2]. Carbon nanotubes were born. A few years later single-walled nanotubules were produced [3, 4].

Carbon nanotubes excited interest in nanoscale materials research mainly be-cause of their unusual electronic structure [5, 6]. This lead to extensive research of carbon nanotubes as components of nanoelectronic devices. The superiority of nanotubes over silicon-based technology has been demonstrated in transistor-like devices [7]. Nevertheless the progress of electronics based in nanotubes is held back by the lack in high quality mass production methods and in controlling the conductivity properties during the synthesis. Also, an improved electric contact to electrodes and other surrounding media is still pursued.

As the carbon nanotube technology has matured, more interest is paid on the

fact that these miniature tubes are the tiny brothers of carbon fibers and inherit the mechanical strength. In fact, due to high level of perfection the tubes have mechanical properties superior to most materials [6]. Carbon nanotubes have an axial Young's modulus in the 1 TPa regime and tensile strength of about 60 GPa [5, 6]. The corresponding values for commercial steel are about 200 GPa for the Young's modulus and 500 MPa for the tensile strength [8], which makes carbon nanotubes five times stiffer and over hundred times tougher than steel. Carbon nanotubes show also remarkable flexibility and capability to recover from extreme mechanical bending or buckling [5, 6]. Besides this the smooth graphene surface exhibits interesting tribological properties. The structural and mechanical properties of carbon nanotubes have lead to research in nanotube-based nanoelectromechanical devices. The tubes can be also used as reinforcement fibers, like carbon filaments, and this has lead to progress in nanotube-polymer composites. In the current view it appears that high performance mechanical applications may be where the near-future of carbon nanotubes lies because electronic applications for carbon nanotubes require much more control over the growth process.

The contribution of this thesis to the nanotube field lies in the studies of structural and mechanical properties of carbon nanotubes. The thesis presents the results of a series of computational and theoretical studies of strained and defective carbon nanotubes. The employed simulations tools are empirical potential and tight binding molecular dynamics simulations. Novel results concerning local curvature induced strain and defects are presented. Defect-free nanotube surface is an extremely low friction surface with high chemical stability. This may prove problematic for applications in which the function relies on conveying mechanical load to the nanotubes, for example, in polymer composites. Nanotube tribology and the role of defects are examined in view of employing the tubes as reinforcement fibers. Irradiation and irradiation induced defects are proposed as a means of tailoring the mechanical properties of nanotubes. The thesis presents an extensive study of defects and strain induced local changes encompassing single-walled tubes, multi-walled tubes and bundles of nanotubes.

The thesis consists of an overview and the publications. The overview aims at giving a general perspective to the field and employed methods thus setting the landscape for the research and the results presented in the publications. The overview begins with an introduction to carbon nanotubes that covers the current state of the field. Chapter 3 discusses atomistic simulations methods. The methods employed in this thesis are covered in detail. A summary of the results is given in Chapter 4. In addition, the publications are referred to, where appropriate, in the rest of the overview.

Chapter 2

Carbon nanotubes

Carbon nanotubes are molecules that consist of pure carbon. They can be thought of as a graphite sheet that has been rolled into a seamless tubule. If the tube is formed of a single graphite layer, graphene, it is called single-walled while multi-walled carbon nanotubes (MWNTs) are formed of several co-axial shells one-inside-another. Typical diameters for single-walled carbon nanotubes (SWNTs) are between 1 nm and 2 nm, and for MWNTs tens of nanometers. The length of carbon nanotubes lies between hundreds of nanometers and millimeters, although the synthesis of even centimeter-long tubes [9, 10] is possible. SWNTs readily bundle into a triangular lattice in which the individual tubes are bound together by van der Waals forces. The inter-tube separation in a nanotube bundle or in a MWNT is close to 0.34 nm, the graphite interlayer distance [5, 6]. Figure 2.1 shows examples of carbon nanotube structures.

2.1 Various types of carbon nanotubes

Since the accidental discovery of carbon nanotubes various production methods have been developed and later on improved. Carbon nanotubes are produced by three main techniques, arc discharge, laser ablation and chemical vapor deposition (CVD). Arc discharge synthesis is based on creating carbon vapor between two carbon electrodes by introducing an arc discharge between them. Nanotubes form from the resulting vapor. Laser ablation methods use a high-energy laser-beam to dissolve the molecules of a carbon based feedstock gas. The decomposed carbon molecules reform into nanotubes. Chemical vapor deposition, on the other hand, is based on feeding in gas phase material which then reconstructs to form the tubes. Arc discharge and laser ablated tubes used to be superior in quality to tubes grown by CVD methods but in the recent years CVD grown tubes have improved in quality and can be almost as good. The reason for the improvement is the scalability of CVD processes. Most of the interest in nanotube
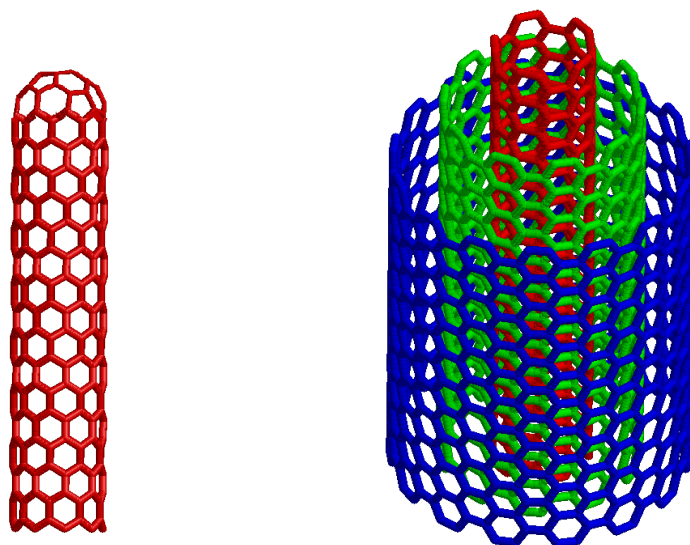
Figure 2.1: Examples of carbon nanotube structures. The nanotubes can be capped as the SWNT on the left. The MWNT on the right has been left uncapped to clarify the nested structure.

synthesis has turned on methods that are potentially extendable to continuous or large-scale production – for example, on CVD. This has resulted in significant improvement in both the CVD tube quality and in the controllability of the CVD processes. Despite this there remains work to be done before these methods are up to controlled mass production. Simultaneously novel scalable methods based on, for example, combustion are pursued.

Currently the carbon nanotube synthesis is at a stage where the synthesized tubes are of high quality and novel gas-flow CVD synthesization methods enable centimeter-long nanotubes [9, 10]. We can control tube growth sites by selective catalyst placement [11, 12], and partially also the type of tubes produced [6]. The current challenges in nanotube production lie in developing a method that combines a scalable process with low-cost, high-quality product with control over the diameter, length and conductivity.

There are numerous ways to roll a graphene sheet to a tube and the resulting structures are most commonly classified by an index pair (n, m) that defines the tube structure in a unique way. The details of this common nanotube classification scheme can be found in Appendix A. The pair of indices (n, m) defines the chirality, that is, how the hexagons formed by carbon atoms are oriented with respect to the tube axis. There exist two possible high symmetry structures for nanotubes known as the zigzag, $(n, 0)$, and the armchair, (n, n). The names

derive from the pattern formed when a particular tube is cut perpendicular to the axis. The indices can be employed to determine the electronic structure of an SWNT [5]. Depending on the combination of the indices, the tube can be metallic or semiconducting [5]. The rolled graphene layer is not, however, all: Unless chemically treated or sonicated, the tubes usually come capped by a hemi-fullerene. The fullerene caps contain pentagons that close the nanotube structure.

In practice the tubes have defects and deviate from the theoretical perfect structure that was discussed above. For example, vacancies, various non-hexagonal rings and the Stone-Wales defect, which is a complex of two pentagons and two hexagons, have been considered. The whole nanotube morphology can change because of these imperfections, for example, nanotubes in a spiral telephone-cord-like form can be synthesized [13, 14]. The μm sized rings observed in Refs. [15, 16] are interesting nanotube structures. At first atomic force microscope (AFM) measurements indicated that the rings were coils instead of closed tori [17] but later evidence of SWNTs that formed closed rings was reported [18].

2.2 Electronic properties

This thesis contributes to the understanding of the mechanical properties of nano-tubes and therefore the electronic properties will be treated only briefly and to cover the major aspects. The electronic structure of carbon nanotubes is unique in materials science. A minor change in the structure can determine whether the tube is semiconducting or metallic. The conductivity of an SWNT is governed by its electronic structure which is determined by the index combination (n, m). For MWNTs the situation is more complex because the multiple layers contribute to the conductivity. Currently, most of the interest in the nanotube electronic trans-port focuses on individual tubes. Bulk transport may be interesting in conducting composites but the main interest is in devices based on individual tubes. The tubes show both ballistic and diffusive transport character depending on the level of perfection of the tubes. SWNTs are more typically ballistic while MWNTs are diffusive because of a higher defect concentration [19].

The effect of defects and deformations on nanotube conductivity has been studied in Refs. [20–27]. Defects in carbon nanotubes act as local scattering centers for charge carriers. The scattering effects of isolated point-defects are averaged over the circumference. Therefore their influence decreases with an increasing diameter and is small for all but the very thinnest tubes. However, if the defects or deformations accumulate locally a tunneling barrier may form. Two tunneling barriers close to each other in a thin wire such as a nanotube form a single electron transistor. This has been exploited in experiments where sharp bends [28, 29] and ion irradiation [30] have been employed for forming tunneling barriers.

Semiconducting behavior has been observed for individual SWNTs. In MWNTs or conglomerations of SWNTs there are usually both semiconducting and conducting layers [31] which makes the pure semiconducting behavior rare in the measurements involving multiple nanotube shells. Currently the development of nanotube based electronics devices has reached the stage where nanotube devices have been demonstrated to behave superior to silicon devices [7]. Mass production schemes are still lacking.

2.3   Mechanical properties

Although the electronic properties and their potential tunability have enticed the scientific community, nanotubes also possess remarkable mechanical properties. These are less sensitive to chirality than the electronic properties and as such more easily exploited *en masse* while the control over the synthesis is not complete enough to provide tubes with desired electronic band structure. The mechanical properties of carbon nanotubes are closely related to the properties of a graphite sheet even though the tubular anisotropy affects the behavior of carbon nanotubes. The basis is the graphite sp^2-bond which is one of the strongest chemical bonds. In nanotubes the overall density of defects can be extremely low depending on the synthesizing method and prevailing synthesizing conditions. This has led to predictions of a very high axial strength and ultra-low friction between the shells.

2.3.1   Mechanical strength

The small size of carbon nanotubes presents challenges for experimental characterization. Nevertheless measurements have been performed. The first Young's modulus measurement [32] related thermal vibration amplitudes of MWNTs to their Young's modulus and obtained an average value of 1.8 TPa with a large spread. After that, with AFM techniques, values such as 1.28 ± 0.59 TPa for arc-discharge produced tubes have been obtained [33]. The latest measuring technique is by Poncharal *et al.* who have induced vibrations on MWNTs by alternating electric potential and measured the vibration frequencies [34]. They report Young's modulus values between 0.7 TPa and 1.3 TPa for tubes with a diameter less than 12 nm and between 0.1 TPa and 0.3 TPa for thicker tubes. This large drop is explained by an onset of a wavelike bending mode of the nanotube [34]. Measuring SWNTs is more complicated than measuring MWNTs due to their small diameters and the tendency to bundle. Krishnan *et al.* report in Ref. [35] a measurement of individual SWNTs using the thermal vibration method of Ref. [32] and they obtain an average value of 1.25 TPa. Although the current measurements suffer from inaccuracies due to vibration amplitude measurement and assumptions made on AFM tip characteristics, the current agreement is that

both SWNTs and MWNTs have a Young's modulus value around 1 TPa. This is extremely high and sets nanotubes as the strongest known material albeit challenged by other nanotubular structures such as boronnitride tubes [6].

Theoretical calculations of axial Young's modulus for individual SWNTs give results around 1 TPa or slightly higher [36, 37]. Most of the theoretical attention has been on SWNTs because the intertube interactions are weak in MWNTs and thus less important in estimating axial mechanical properties. In Ref. [37] Lu presents Young's modulus values for MWNTs as well as SWNTs and obtains values from 0.97 TPa to 1.11 TPa with the value increasing slightly with the number of layers. In this thesis the theoretical discussion on nanotube strength is extended to the influence of defects on the Young's modulus. The research reported in Publication V indicates that point-defects have little influence on the Young's modulus. This may explain the excellent agreement between the theoretical estimates concerning pristine tubes and the measurements in which the nanotubes are likely to contain defects.

Measurements of tensile strength, that is, the strength corresponding to failure, suffer from difficulties and inaccuracies related to the small size of the measured object. Tensile strength has been measured for MWNTs in Ref. [38] where the contact is only to the outmost layer of the multi-walled tube. A sword and sheath type of failure of this layer was reported. The tensile strength values ranging from 11 GPa to 63 GPa were reported [38]. For individual SWNTs the experimental value of tensile strength is still an open question but for bundles of SWNTs tensile strength values ranging between a few GPa and several tens of GPa depending on the bundle and measurement characteristics have been reported [39–41].

Theoretical tensile strength of nanotubes is high [42–45]. The measurements fall short of the theoretical predictions which may result from limitations in the theoretical description or from the presence of imperfections in the structure. The simulations suffer from restricted time scales and model-related limitations, such as the cut-off problem [43]. The difference between the results of the theoretical works and the experiments can also be partially explained by the work done in this thesis in Publication V. The results show that even a single point-like structural imperfection in an otherwise perfect nanotube can deteriorate the mechanical strength to a fraction.

Even though not as strong as theoretically expected, the tubes still have an extremely high tensile strength. As a result of this, nanotubes can bear large strain before plastic deformation or brittle failure. The tubes can buckle, flatten, form ripples, and generally deform under strain [46–48] but plastic deformation and relaxation can occur only at elevated strain levels and temperatures [49–51]. These aspects are discussed in more detail in Publications I-III.

The high axial Young's modulus and tensile strength combined with the low weight and fiber-like form make nanotubes enticing candidates for composite reinforcement. Composites of nanotubes are based on dispersing nanotubes into
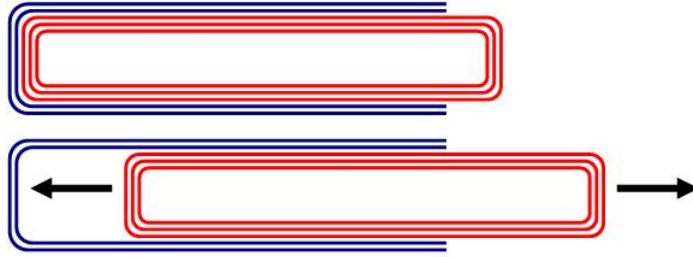
Figure 2.2: A schematic presentation of a nanotube oscillator. The inner tubes slide with respect to the outer shells almost friction-free.

a matrix of material that acts as the main body of the composite. The nanotubes are the reinforcement fibers and improve the overall mechanical strength of the composite. With the improved treatment and manipulation techniques, promising results concerning nanotubes in a polymer matrix, that is, nanotube–polymer composites, have emerged [52–54].

2.3.2   Low-friction surfaces of carbon nanotubes

Carbon nanotubes have extremely strong covalent bonding of atoms within the shells but very weak van der Waals type interactions between them [6]. The covalent sp^2-type bonding results in exceptional axial strength for individual nanotubes. On the other hand, the weak inter-shell interactions combined with low defect concentrations indicate that the surfaces of the tubes slide easily with respect to each other, that is, the tubes are low-fiction surfaces. These anisotropic mechanical properties imply a broad range of possible applications as constituents of nanometer-scale devices and novel composite materials.

The low-friction behavior can potentially be exploited in MWNT based low friction components of nanomechanical devices. Indeed, as recent experimental [55–58] and theoretical [59–63] studies demonstrate, the individual cylinders of MWNTs easily slide or rotate with respect to one another. Linear bearings with ultra-low friction have been implemented [55] and an electromechanical device [64] in which the operation is based on the low-friction properties of the MWNTs has been demonstrated. These properties can also be utilized in MWNT-based oscillators [60–63, 65] with operating frequencies up to several gigahertz. Figure 2.2 shows a schematic presentation of a nanotube oscillator.

The easily sliding surfaces can also be detrimental for applications. A low-friction surface indicates that mechanical load transfer is inefficient. This can be detrimental in various reinforcement applications. These questions are addressed in Publications IV-VI.

2.3.3 Defects and mechanical properties

Nanotubes can have an extremely low defect density and many of their key properties, for example, the long electron scattering lengths and the ultra-low friction discussed above are based on this property. Despite this, as in any material, defects play an important role in nanotube properties. Defects act as scattering centers for charge carriers. They also make the tube less strong and thus defects are rarely desirable from the purely mechanical point of view. Defects are generated in the synthesizing process and they can also be caused by, for example, ion or electron beam irradiation of the tube, or mechanical manipulation. The most typical structural defects are fivefold (pentagon) and sevenfold (heptagon) rings in the sixfold (hexagonal) lattice. Other types of typical defects are vacancies, interstitials and miscellaneous bonding configurations such as locally amorphous structure. Non-carbon based defects include substitutional atoms or atom groups. In addition to these, MWNTs exhibit diverse defects related to irregularities in the layered structure. Defects may alter the tube form from a straight tube to a bulging, kinked, spiral or even more miscellaneous form [5, 6]. Figure 2.3 shows examples of defects in nanotubes.

In Publications IV-VI of this thesis the aspect of employing defects, more precisely irradiation induced defects, to manipulate mechanical properties is studied. We propose and show that defects can be employed to improve load transfer between the low-friction surfaces of the nanotubes. This enables improved mechanical properties for applications such as nanoelectromechanical devices or polymer composites in which tube-tube-slippage may be detrimental.

2.4 Irradiation and carbon nanotubes

Because the second part of this thesis, Publications IV-VI, concentrates on evaluating the effects of irradiation induced damage on nanotube mechanical properties, an overview of irradiation based carbon nanotube research is presented here. In many ways the bombardment of carbon nanotubes with energetic electrons or ions gives rise to similar results as in graphite [66] but there are also subtle differences because of the all-surface structure of a carbon nanotube [67].

When a material is irradiated, the dominant energy transfer method can be kinetic energy transfer to the nuclei, electronic excitations, electron knockouts, etc. depending on the incident particle and on the target material. In carbon nanotubes atomic knock-out displacements dominate the process [6]. This creates single and multiple vacancies and a corresponding number of sputtered atoms, which can, if energetic enough, knock out additional particles. Because of the one dimensional structure, the sputtered atoms can propagate out from the tube thus reducing the number of potential interstitial atoms. The remaining interstitials can be treated as adatoms [68, 69] on the tube surface because of the large tube-tube
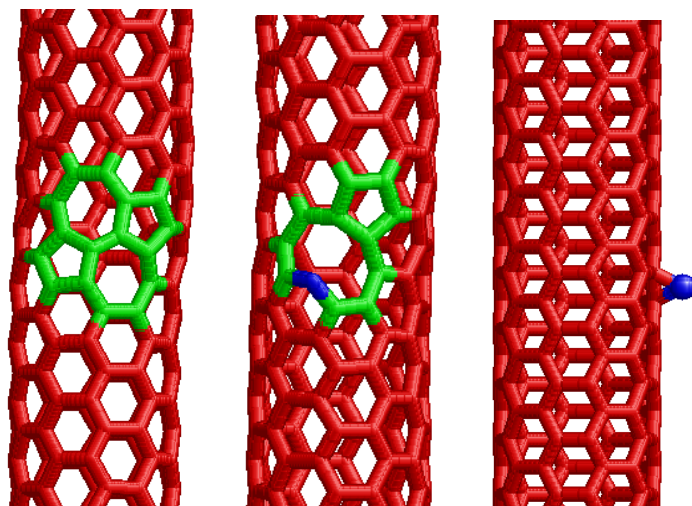
Figure 2.3: Examples of defects in nanotubes. The leftmost image shows a Stone-Wales defect that has been given much consideration in nanotubes. It consists of a complex of two pentagons and two heptagons and is formed by a bond rotation from the hexagonal lattice. The center image shows a vacancy structure in which two of the dangling bonds in the vacancy have reconstructed to form a pentagon and the remaining dangling bond (blue) protrudes from the surface. The image on the right shows an ad-atom on the surface of a nanotube.

separation. The structure enables the sputtered atoms to propagate far from the collision site even though the incident beam energy would be only slightly above the knockout threshold. Therefore, once created the vacancy–ad-atom pairs, that is, the Frenkel pairs, are not likely to recombine instantaneously [67]. Figure 2.4 shows a knock-out process that results in the formation of a Frenkel pair.

Carbon nanotubes behave differently from a bulk material when the irradiation damage is annealed. Because vacancies and sputtered atoms can be separated in distance, recombination annealing does not take place to such an extent as in bulk materials. There appears to be two annealing mechanisms: vacancy healing through the saturation of dangling bonds which results in non-hexagonal rings and interstitial migration which results in recombination of the defects [67].

Both electron and ion irradiation have been employed in carbon nanotube research. Electron irradiation has been employed to modify nanotube structure [70–73], for example, to coalesce nanotubes [71] and to weld the tubes together to form molecular junctions [72], which provides interesting prospects for nanoelectronics. Figure 2.5 shows an example of irradiation-induced welding of carbon nanotubes. Ion-irradiation has been employed for example to form tunnel barriers [74], to induce inter-tube links [75] and for chemical functionalization [76].

Irradiation induced defects have been demonstrated to induce inter-tube links
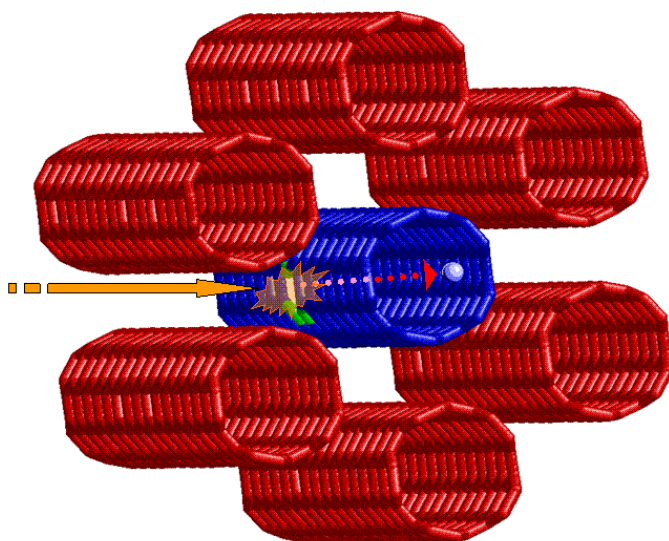
Figure 2.4: A visualization of an irradiation knock-out process in a carbon nanotube bundle. The displaced atom can be seen moving in the axial direction.
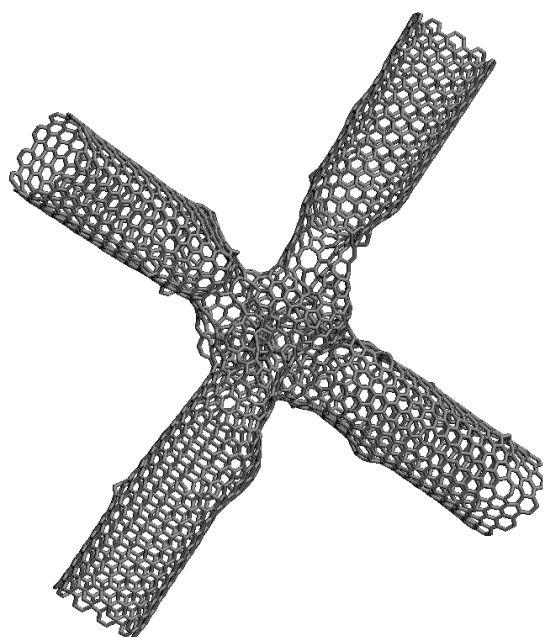
Figure 2.5: An example of irradiation-induced welding of nanotubes. The irradiated nanotubes have coalesced to form a cross-junction. The figure is provided courtesy of Arkady Krasheninnikov.

[66, 75, 77–79] and to bind graphite layers [80]. Such links are likely to be effective in load transfer as reported in Publications IV and VI. Simultaneously, carbon nanotubes show evidence of remarkable self healing of damage [69] and the results of Publication V show that this compensates largely for the defect-induced structural weakening. With the current results on functionalization [76, 81] and load transfer [75, 79] it appears reasonable that bombardment with energetic particles may be employed to tailor nanotube properties and reactivity with the environment. Besides this, irradiation has prospects in the electronics sense: It enables controlled nanowelding of the tubes, tunnel barrier formation, and potentially also improved contacts.

Chapter 3

Simulation methods

A rigorous calculation of the properties of a system at the atomistic scale is based on solving the many body time dependent Schrödinger equation and obtaining the many body wave function $\Psi(r_1, \ldots, r_n, t)$. Unfortunately, exact analytical solutions exist only for a handful of cases such as the hydrogen atom and the harmonic oscillator. Numerically the problem is intractable for systems containing more than a few particles. The exponentially rising demand of computational resources ensures that exact quantum mechanics is not to be considered as a way to solve condensed matter problems. Researchers have to rely on approximations of various orders of the Schrödinger equation and even on totally classical empirical approaches.

This chapter offers first an overview on the approximations, *i.e.*, on materials simulation methods at atomic scale. The survey is presented in Section 3.1. In this thesis the emphasis is on classical molecular dynamics and empirical carbon modeling by the Brenner interaction model [82] and its long range extension by Stuart *et al.* [83]. Therefore these are discussed in detail followed by an introduction to the density functional theory based tight binding method [84, 85] employed in Publication III.

3.1 Introduction

The methods of modeling the atomic interactions can roughly be divided into three categories: The first principles, or *ab initio*, methods are the most rigorous ones. Only a few well controlled approximations to exact quantum mechanics are made. Semiempirical methods contain more drastic approximations and may also contain empirically defined parameters. Empirical methods are a group of methods that are tuned to reproduce an empirically defined fitting set. The three categories, their drawbacks and benefits, and the most popular methods of each are briefly described in this section.

3.1.1   First principles methods

The most rigorous approach to problems of condensed matter physics are the first principles methods. They do not employ any empirical parameters in the calculation. The results are based on quantum mechanics and well controlled approximations. The two most used first principles methods are the Hartree-Fock method [86] and the density functional theory [87, 88]. The first principles methods are highly accurate but the system size that can be handled is restricted to tens, at most a couple of hundred atoms.

The Hartree approach to the quantum mechanical many body wave function is to approximate the function by a product of single particle functions. The approximation is refined by adding Fermi–Dirac statistics by replacing the product of the wave functions by the Slater determinant. The method obtained with this inclusion is called the Hartree–Fock approach [86]. Even though the method is not always extremely accurate, it is much used. The accuracy can be enhanced but this increases the consumption of CPU-time [89]. In its most rigorous form, the Hartree–Fock method can be used on systems of tens of atoms.

Density Functional Theory (DFT) [87, 88] is based on using the electron density $n(\vec{r})$ of the system as the basic variable. The ground state is completely described by the electron density as stated by the Kohn–Sham theorem [87, 88]. There are various schemes of determining the energy of the system from the electron density. In the most simple form of DFT, in local density approximation (LDA), the expressions based on a non-interacting electron gas at the local electron density of the real system. Currently DFT is a very accurate method and its accuracy can be enhanced by the use of methods combining Hartree–Fock and DFT description, for example, B3LYP[1] functional description [89]. DFT can be used on systems of a few hundred atoms.

3.1.2   Semiempirical methods

Semiempirical methods employ various approximations and may include experimentally fitted parameters. Their power with respect to the first principles methods lies in a smaller consumption of CPU-time but they must be employed more carefully to obtain reliable results. Semiempirical methods include interaction schemes like the tight binding method (TB) [90] and various molecular orbital methods of computational chemistry [89].

The tight binding method avoids most of the heavy calculation of the *ab initio* methods. There are several methods in this family. The TB-methods have in common a number of simplifications such as minimal basis sets compared to the first-principles methods and elimination of difficult integrals, that are either

---

[1]B3LYP is short for **B**ecke's **3**-parameter formula, B3, which describes the exchange functional, and LYP for **L**ee, **Y**ang, and **P**arr who developed the correlation functional [89].

made small by mathematical transformations or used as parameters to be fit to experimental data. In principle, everything that can be calculated by the *ab initio* methods can be calculated by an appropriate tight binding method and with less CPU-time. The keyword above is the 'appropriate': the generality and the transferability of a tight binding method depend on the approximations. Although valid for thousands of particles, the method used must be assessed case-specifically.

In computational chemistry the methods similar to tight binding are called the neglect of diatomic differential overlap methods [89]. Also these methods simplify the involved integrals but retain the molecular orbital description. The group involves various methods such as AM1[2] and PM3[3] [89].

3.1.3 Empirical methods

The category of empirical methods contains a wide set of parametrized classical force fields that reproduce more or less accurately the fitting set that is determined either from experimental data or from *ab initio* simulations. Force-field methods have the benefit of being computationally simple and thus fast. They allow the simulation of large systems (up to hundreds of millions of atoms) over a greater time-span (up to microseconds) than the methods presented above.

The simplest approximation for the interaction potential takes into account only two-particle interactions. Potentials like this are called pair potentials. The Lennard-Jones potential [91] and the Morse potential [92] are two very well known examples of pair potentials. Although pair potentials are not ideal for the study of the mechanical properties of materials, they are very much used because they are simple to implement and algorithms based on pair potentials are kind on computational resources. There are, however, some severe shortcomings which should be taken into account whenever pair potentials are used. For example, an interaction described by a pair potential model can depend only on the distance between the two particles. Thus the potential can not model directional bonding. Pair potentials often predict wrong vacancy formation energies and melting temperatures [91, 92].

The construction of an accurate force-field encounters often system and material based difficulties, and often even fundamental limitations. Difficult media are metals, alloys, semiconductors, and oxide-based insulators. In this thesis the emphasis is, of course, on carbon. Describing carbon accurately requires a lot of caution and is difficult because the $2s$ electrons participate in molecular bonding and together with the $2p$ electron orbitals hybridize to form a wide variety of potential bonding configurations that depend on the environment and on the ambient conditions. Even by itself, carbon can form structures as diverse as the

---

[2]**A**ustin **M**odel **1** is named after the place of its origin, that is, University of Texas, Austin, USA.

[3]**P**arametrized **M**odel **3** is named so because it was the third parametrized model released by the person in charge for its development.

isotropic diamond crystal or the anisotropic planar graphite and nanostructures. If the consideration is extended to organic molecules, even only hydrocarbons, the bonding variety, and at the same time the complexity of describing it accurately, becomes vast.

If covalently bonding materials, like sp^2-carbon, are simulated, the modeling of directional bonding is essential in order not to obtain outright wrong results. In general this means that the interaction potential used must include at least a three-body interaction term. Because carbon is the basis of all organic materials and because diamond and graphite have various applications in materials science, numerous attempts to create accurate classical interaction potentials have been made but only a few of the proposed schemes are widespread. For example, carbon interaction potentials developed by Tersoff in Refs. [93–95] and Brenner in Ref. [82] are widely used in the modeling of carbon. The Brenner model is considered more versatile because of additional conjugated bond description while the structures modeled by the Tersoff model suffer from an overbinding of radicals and the description of systems involving bonds that exhibit a mixture of sp^3 and sp^2 hybridization is inaccurate. Both models are short ranged and cover only the nearest neighbors to speed up the calculations. For description of graphite or multi-walled nanotubes, much longer range interactions are required. Various long-range extensions that are most often based on Lennard-Jones type additional term to describe the π-bonding have been proposed. Stuart *et al.* [83] have aimed at maintaining the reactivity description of the Brenner [82] model while introducing the long-range interactions. Therefore, this model was chosen where long-range interactions are required.

In general the force-field methods can give information on the structure and dynamics of a system, the total energies, entropies, free energies, and diffusive processes in the system. By their construction the methods are incapable of predicting any properties related to the electronic structure such as electrical conductivity, optical, or magnetic properties. In short, the classical force field methods are structural tools. The general accuracy of results obtained by classical force field methods is far from the level of accuracy obtained by *ab initio* simulations but so are the feasible system size and attainable time scale as well.

3.2   Methods employed in this thesis

In this thesis the emphasis is on studying carbon nanotube properties through classical means. The choice allows studying structures that have dimensions comparable to the experimentally observed ones. Classical molecular dynamics [91] with Brenner's hydrocarbon potential [82] and in Publications IV and VI Stuart's extension to it [83] are employed in the simulations. In Publication III a density functional theory based tight binding model is employed [84, 85]. A molecular

dynamics program with an interactive graphical interface was implemented for Publications I-III by the author. This program incorporates Lennard-Jones interaction model and Brenner carbon-carbon interaction model. For Publications IV-VI, another program implemented in the Accelerator Laboratory of University of Helsinki has been used. The program carries the name Parcas and in the following it will be referred to by this name. Parcas was originally implemented for the study of ion bombardment of materials and a vast number of interaction models and parametrizations have been incorporated to it. For the tight binding calculations a tight binding implementation developed in the group of Prof. Frauenheim at the University of Paderborn has been used. Next the relevant aspects of these methods for the research presented in this thesis are discussed.

3.2.1 Classical molecular dynamics

If phenomena are studied classically in the atomistic scale there are two concurrent simulation methods. Classical Monte Carlo methods are based on treating a mathematical problem by finding a probabilistic analogue and then solving it by stochastic sampling. The basic Monte Carlo algorithm is called the Metropolis Monte Carlo and is described in Refs. [92, 96]. The second method, the classical molecular dynamics (MD) method, is a deterministic method and this was chosen for the work. The basic concept of an MD simulation is to simulate the time evolution of a system. In classical MD the atoms are considered as point-like masses that interact according to a given potential energy $V(\vec{r}_1, \vec{r}_2, \ldots, \vec{r}_N)$. The evolution is computed in steps of a small time period δt and is thus discrete. The essential quantity to be known is the potential energy, since a system of interacting classical particles obeys Hamiltonian dynamics and consequently Newton's equation of motion

$$\vec{F}_i = m \frac{d^2 \vec{r}_i}{dt^2} = -\nabla_i V(\vec{r}_1, \vec{r}_2, \ldots, \vec{r}_N), \qquad (3.1)$$

where the index i refers to one of the N particles in the system [91].

Integration of the equations of motion

In order to find out, how the system evolves in time, the equation of motion must be solved for each particle. This is called the integration of the equation of motion. There are several integration schemes of various complexity and order [91, 92], but the discussion is limited to the ones employed in this thesis.

A Verlet leapfrog algorithm has been chosen for the program that was developed for the study because of the simplicity and relative stability of the algorithm in comparison to other integration algorithms [91]. Also the regular Verlet integration algorithm [92] was implemented but the numerical stability was not as good as with the equivalent leapfrog algorithm.

The integration equations of the Verlet leapfrog algorithm are

$$\begin{cases} \vec{r}_i(\tau + \delta t) = \vec{r}_i(\tau) + \delta t \vec{v}_i\left(\tau + \frac{1}{2}\delta t\right), \\ \vec{v}_i\left(\tau + \frac{1}{2}\delta t\right) = \vec{v}_i\left(\tau - \frac{1}{2}\delta t\right) + \delta t \vec{a}_i(\tau), \end{cases} \tag{3.2}$$

where δt is the integration time step. In order to obtain the new position and the new velocity, $\vec{r}_i(\tau + \delta t)$ and $\vec{v}_i\left(\tau + \frac{1}{2}\delta t\right)$, one must know $\vec{r}_i(\tau)$, $\vec{v}_i\left(\tau - \frac{1}{2}\delta t\right)$, and $\vec{a}_i(\tau)$. It should be noted that the position and the velocity in the algorithm are not computed at the same time.

Next a list-like representation of the workings of a classical molecular dynamics simulation using the Verlet leapfrog integration algorithm is presented.

  I. Set the initial position and velocity distribution at the time $\tau = \tau_0$.

 II. Calculate the accelerations at the current time τ.

III. Calculate the velocities at the time $\tau + \frac{1}{2}\delta t$.

IV. Calculate the new positions and update the positions.

 V. Compute the relevant physical quantities.

VI. Set the current time to be $\tau = \tau + \delta t$.

VII. Go to II and continue looping as long as the simulation is run.

The steps from II to VI represent one molecular dynamics step. The step is repeated and a discrete time development of the system and its dynamics is obtained.

The other classical simulations program employed in the thesis, Parcas, employs the 5th order predictor-corrector Gear integration scheme [92]. This integration scheme is considered computationally heavy with only small improvements to the integration accuracy because of the use of higher order derivatives and the corrector step. The scheme has, however, an accuracy advantage at short time steps and therefore it is used in this molecular dynamics program that was originally developed for ion bombardment simulations in which the particle energies are typically extremely high and thus short time steps are used. The integration equations of the Gear algorithm are based on a predictor step

$$\begin{cases} \vec{r}_i^p(\tau + \delta t) = \sum_{j=0}^{5} \frac{\vec{r}_i^{(j)}(\delta t)^j}{j!} \\ \vec{v}_i^p(\tau + \delta t) = \sum_{j=0}^{4} \frac{\vec{v}_i^{(j)}(\delta t)^j}{j!} \\ \vec{a}_i^p(\tau + \delta t) = \sum_{j=0}^{3} \frac{\vec{a}_i^{(j)}(\delta t)^j}{j!} \\ \vec{b}_i^p(\tau + \delta t) = \sum_{j=0}^{2} \frac{\vec{b}_i^{(j)}(\delta t)^j}{j!} \\ \dots \end{cases} \tag{3.3}$$

which is corrected by a following corrector step. The predicted positions $\vec{r}_i^p(\tau + \delta t)$ are used to compute the corrected accelerations $\vec{a}_i^c(\tau + \delta t)$. The acceleration correction becomes:

$$\Delta \vec{a}_i(\tau + \delta t) = \vec{a}_i^p(\tau + \delta t) - \vec{a}_i^c(\tau + \delta t).$$

(3.4)

The corrected positions, velocities, *etc.* can now be written

$$
\begin{cases}
\vec{r}_i^c(\tau + \delta t) = \vec{r}_i^p(\tau + \delta t) + c_0 \Delta \vec{a}_i(\tau + \delta t) \\
\vec{v}_i^c(\tau + \delta t) = \vec{v}_i^p(\tau + \delta t) + c_1 \Delta \vec{a}_i(\tau + \delta t) \\
\vec{a}_i^c(\tau + \delta t) = \vec{a}_i^p(\tau + \delta t) + c_2 \Delta \vec{a}_i(\tau + \delta t) \\
\vec{b}_i^c(\tau + \delta t) = \vec{b}_i^p(\tau + \delta t) + c_3 \Delta \vec{a}_i(\tau + \delta t) \\
\dots
\end{cases}
$$

(3.5)

A detailed discussion of how to choose the coefficients c_i can be found in Refs. [97, 98]. In a schematic form the Gear integration algorithm works as follows

  I. Set the initial positions at the time $\tau = t_0$.

 II. Calculate the predicted positions, accelerations, *etc.* at the time $\tau + \delta t$ using the current values of each quantity.

III. Calculate the correction to the acceleration based on the predicted positions.

IV. Correct the predicted values of positions, accelerations, *etc.*.

 V. Compute the relevant physical quantities.

VI. Set the current time to be $\tau = \tau + \delta t$.

VII. Go to II and continue looping as long as the simulation is run.

For the beginning of the simulation the initial position distribution, the initial velocity distribution, and the initial time step value must be set. For the simulation of solids, an appropriate initial position distribution is, for example, the lattice structure the particles form in nature under the prevailing physical conditions of the simulation. The initial velocity distribution defines the temperature and the momentum of the system. The time step δt must be set so that the particle movement in one step is very small compared to the average particle distance. The smaller the time step is the more justified it is to use the force computed at a moment τ as an approximation for the force during the interval $[\tau, \tau + \delta t]$. On the other hand, a too small time step wastes computational resources. Time step length is therefore a compromise between accuracy, stability and speed. Typically the step is approximately 1 fs in equilibrium simulations. For the simulations in this thesis the time step values have been slightly smaller because the structures

have often been distorted and out of equilibrium thus involving larger recuperating forces. It should be noted that all finite δt values induce a drift that increases the total energy of the simulated system unless the energy is kept at level by employing a thermostat algorithm. If the energy drift is detrimental, and thermostating may disturb the results, an unusually short timestep should be used as in the static friction simulations of Publication IV.

Calculating the physical quantities of the system

Classical molecular dynamics simulations allow the calculation of physical properties of the system quite easily. The expressions are in general based on statistical mechanics and averages. The time average of a quantity A is calculated

$$< A_t >= \frac{1}{t} \int_0^t A[x(\tau)]d\tau \ , \tag{3.6}$$

where $x[\tau]$ describes the state of the system at time τ. This expression allows the computation of any physical quantity that can be evaluated momentarily for the system. For example, the total energy of the system at a moment of time τ is given by:

$$E_{\text{tot}}(\tau) = \frac{1}{2} \sum_i m\vec{v}_i(\tau)^2 + \sum_i \sum_{j>i} V\left(\vec{r}_1(\tau), \vec{r}_2(\tau), \ldots, \vec{r}_N(\tau)\right) \ , \tag{3.7}$$

where $V(\vec{r}_1(\tau), \vec{r}_2(\tau), \ldots, \vec{r}_N(\tau))$ stands for the potential energy. It is important to notice that the velocity in the Verlet leapfrog algorithm of Equation (3.2) is not $\vec{v}(\tau)$ but $\vec{v}(\tau + \frac{\delta t}{2})$ instead. The average of two adjanced v values may be used for the computation of the required velocity at a moment τ but the approximation causes some fluctuation in the momentary value of total energy. As another example of computing physical quantities for the system, the local temperature of the system can be obtained from the equipartition theorem. The equipartition theorem states that the part of the kinetic energy associated to each degree of freedom is given by $\frac{1}{2}k_b T$, where k_b is the Boltzmann constant. In a three dimensional system with N point-like masses there are $3N$ degrees freedom and thus

$$T = \frac{2 \langle E_k \rangle}{3k_b N} \tag{3.8}$$

is obtained for the temperature of the system. Here $\langle E_k \rangle$ is the average total kinetic energy of the system [99].

3.2.2   Brenner potential energy model

Brenner's hydrocarbon potential energy model [82], which is based on Abell's [100] and Tersoff's [93–95] bonding formalism and interaction models, was chosen for

the work. The interaction potential has previously given better results in describing sp^3-bonding than Tersoff's carbon potential energy model, which suffers from overbinding of atoms [101]. The bonding in carbon nanotubes is mainly graphitic sp^2-bonding, but there is also some sp^3-bonding present, and thus Brenner's potential energy model was chosen over Tersoff's formulation. When previously used on carbon nanotubes, Brenner's parameterization has given results that are in excellent agreement with corresponding tight binding computations [49, 50, 102, 103].

The Brenner potential energy model is an empirical many body interaction potential developed for hydrocarbons. The basic formulation is that of Tersoff's but some additional terms are introduced to correct for the overbinding of radicals and for taking into account nonlocal effects in the system. This section introduces the Brenner model while the detailed mathematical treatment of computing the forces is left to Appendix B.

The binding energy in the Brenner bond order potential energy model is given by a sum over the bonds:

$$E_b = \sum_i \sum_{j>i} \left[V_R \left(r_{ij} \right) - \bar{B}_{ij} V_A \left(r_{ij} \right) \right] , \qquad (3.9)$$

where V_R represents the repulsive part of the interaction and V_A the attractive part. Here the empirical bond-order function is given by

$$\bar{B}_{ij} = \frac{1}{2} \left(B_{ij} + B_{ji} \right) + \frac{1}{2} F_{ij} \left(N_i^{(t)}, N_j^{(t)}, N_{ij}^{conj} \right) , \qquad (3.10)$$

where F_{ij} represents the correction for overbinding, and the attractive and the repulsive pair terms are given by

$$V_A \left(r_{ij} \right) = f_{ij} \left(r_{ij} \right) \frac{D_{ij}^{(e)} S_{ij}}{S_{ij} - 1} e^{-\sqrt{2/S_{ij}} \beta_{ij} \left(r_{ij} - R_{ij}^e \right)} , \qquad (3.11)$$

and

$$V_R \left(r_{ij} \right) = f_{ij} \left(r_{ij} \right) \frac{D_{ij}^{(e)}}{S_{ij} - 1} e^{-\sqrt{2 S_{ij}} \beta_{ij} \left(r_{ij} - R_{ij}^e \right)} , \qquad (3.12)$$

in which the function $f_{ij} \left(r_{ij} \right)$ is the cut-off function that restricts the pair interaction to the nearest neighbors and r_{ij} is the interatomic distance of particles i and j. $D_{ij}^{(e)}$, S_{ij}, R_{ij}^e, and β_{ij} are experimentally fitted parameters. The values of the parameters are given in Appendix B. The cut-off function drives the interaction smoothly to zero at a given interval $\left[R_{ij}^{(1)}, R_{ij}^{(2)} \right]$:

$$f_{ij} \left(r_{ij} \right) = \begin{cases} 1, & \text{if } r_{ij} < R_{ij}^{(1)} \\ \frac{1}{2} \left[1 + \cos \left(\frac{\pi \left(r_{ij} - R_{ij}^{(1)} \right)}{R_{ij}^{(2)} - R_{ij}^{(1)}} \right) \right] , & \text{if } R_{ij}^{(1)} < r_{ij} < R_{ij}^{(2)} \\ 0, & \text{if } r_{ij} > R_{ij}^{(2)} , \end{cases} \qquad (3.13)$$

where $R_{ij}^{(1)}$ and $R_{ij}^{(2)}$ are the cut-off radii. The presence of a cut-off function intro-duces an artefact related to overestimating the interparticle forces at interparticle distances in the cut-off range [43, 101, 104]. This must be taken into account in the simulations and the topic is discussed in the related Publications IV and V.

In Equation (3.10) the empirical bond-order term B_{ij} reads as

$$
B_{ij} = \left[1 + \sum_{k \neq i, j} G\left(\theta_{ijk}\right) f_{ik}\left(r_{ik}\right) e^{\alpha_{ijk}\left[\left(r_{ij}-R_{ij}^{(e)}\right)-\left(r_{ik}-R_{ik}^{(e)}\right)\right]} \right.
$$
$$
\left. + H_{ij}\left(N_i^{(H)}, N_i^{(C)}\right) \right]^{-\delta_{ij}}
\tag{3.14}
$$

for hydrocarbons. The expression is simplified in the absence of hydrogen. If, as in the case studied here, only pure carbon is present the parameter $\alpha_{jk} = 0$ and the hydrogen bonding function H_{ij} is zero for all (carbon) particles i, j, and k. The expression becomes

$$
B_{ij} = \left[1 + \sum_{k \neq i, j} G\left(\theta_{ijk}\right) f_{ik}\left(r_{ik}\right) \right]^{-\delta_{ij}} .
\tag{3.15}
$$

The angle θ_{ijk} represents the angle between bonds $i-j$ and $i-k$, and the angle dependent function G is given by

$$
G\left(\theta_{ijk}\right) = a_0 \left(1 + \frac{c_0^2}{d_0^2} - \frac{c_0^2}{d_0^2 + \left(1 + \cos\left(\theta_{ijk}\right)\right)^2} \right),
\tag{3.16}
$$

where a_0, c_0 and d_0 are empirically fitted parameters. Again, the values can be found in Appendix B.

The number of neighbors for an atom is defined to be

$$
N_i = \sum_j f_{ij}\left(r_{ij}\right),
\tag{3.17}
$$

where the cut-off function f_{ij} is used to make the expression continuous. The value of N_i can be used to determine if the atom i is part of a conjugated system. A carbon atom is part of a conjugated system whenever the atom has one or more neighbors, that have a coordination number less than four ($N_i < 4$). A value for describing the conjugated bond between the atoms i and j, N_{ij}^{conj}, is given by

$$
N_{ij}^{conj} = 1 + \sum_{k \neq i, j} \left[f_{ik}\left(r_{ik}\right) F\left(x_{ik}\right) + f_{jk}\left(r_{jk}\right) F\left(x_{jk}\right) \right],
\tag{3.18}
$$

where

$$
F\left(x_{ik}\right) = \begin{cases} 1, & \text{if } x_{ik} \leq 2 \\ \frac{1}{2}\left[1 + \cos\left(\pi\left(x_{ik} - 2\right)\right)\right], & \text{if } 2 < x_{ik} < 3 \\ 0, & \text{if } x_{ik} \geq 3, \end{cases}
\tag{3.19}
$$

and

$$x_{ik} = N_k - f_{ik}(r_{ik}) .$$ (3.20)

When Equations (3.11) and (3.12) are plugged into Equation (3.9) it becomes

$$
\begin{aligned}
E_{\text{b}} = \frac{1}{2} \sum_i \sum_{j \neq i} &\left[\frac{D^{(e)}}{S-1} f_{ij} e^{-\sqrt{2S}\beta(r_{ij}-R^e)} - \frac{1}{2} \frac{D^{(e)}S}{S-1} f_{ij} e^{-\sqrt{\frac{2}{S}}\beta(r_{ij}-R^e)} . \right. \\
&\left. \left[\left[1 + \sum_{k \neq i,j} G(\theta_{ijk}) f_{ik} \right]^{-\delta} + \left[1 + \sum_{k \neq i,j} G(\theta_{jik}) f_{jk} \right]^{-\delta} + F_{ij} \right] \right],
\end{aligned}
$$ (3.21)

where f_{ij} and F_{ij} are shorthand notations for $f_{ij}(r_{ij})$ and $F_{ij}\left(N_i^{(t)}, N_j^{(t)}, N_{ij}^{\text{conj}}\right)$. The parameters S_{ij}, β_{ij}, R_{ij}^e, δ_{ij} and $D_{ij}^{(e)}$ have been replaced by shorter notation S, β, R^e, δ, and $D^{(e)}$ because the indices are unnecessary since only carbon-carbon interactions are considered. Equation (3.21) can now be used to compute the interparticle forces

$$\vec{f}_m = -\nabla_m E_{\text{b}} .$$ (3.22)

The gradient and some additional details concerning the potential energy model are presented in Appendix B.

3.2.3 Stuart potential energy model

The second employed empirical potential energy model, the Stuart model [83] is an extension of the Brenner model [82]. The Stuart model adds torsional potential description of hydrocarbon rotations, and, what is more important for this thesis, describes the long range van der Waals interactions required for the description of graphite interlayer π-bonding or tube-tube interaction in MWNTs or bundles of single walled nanotubes.

Stuart *et al.* maintain the original form and parametrization of the Brenner model [82] whereever possible. The original Brenner energy E_{b} (Eq. 3.21), the dihedral correction E_{tors} and the long-range energy E_{LJ} contribution are considered independent and treated separately:

$$E = E_{\text{b}} + E_{\text{LJ}} + E_{\text{tors}} .$$ (3.23)

The long range interaction is described through a Lennard-Jones (LJ) interaction potential

$$V_{ij}^{\text{LJ}}(r_{ij}) = 4\epsilon_{ij} \left[\left(\frac{\sigma_{ij}}{r_{ij}} \right)^{12} - \left(\frac{\sigma_{ij}}{r_{ij}} \right)^6 \right] .$$ (3.24)

This Lennard-Jones interaction depends on the distance between the atoms i and j, on the strength of their interaction, and on the network of bonds connecting

these atoms. These requirements are described by the additional E_{LJ} term in Equation (3.23):

$$E_{ij}^{LJ} = \left[S\left(t_r\left(r_{ij}\right)\right) S\left(t_b\left(\bar{B}_{ij}^*\right)\right) + 1 - S\left(t_r\left(r_{ij}\right)\right) \right] C_{ij} V_{ij}^{LJ}, \qquad (3.25)$$

where $S(t)$ describes switching the interaction on and off:

$$S(t) = \Theta(-t) + \Theta(t)\Theta(1-t)[1 - t^2(3 - 2t)]. \qquad (3.26)$$

Here $\Theta(t)$ is the Heaviside step function, that is, for $t < 0$ the switching function equals to unity and for $t > 1$ $S(t) = 0$. In between and at the end points the function and the first derivative are continuous. The function $t(r_{ij})$ scales as

$$t_r\left(r_{ij}\right) = \frac{r_{ij} - r_{ij}^{LJmin}}{r_{ij}^{LJmax} - r_{ij}^{LJmin}}, \qquad (3.27)$$

where r_{ij}^{LJmin} and r_{ij}^{LJmax} limit the switching region. These have been chosen $r_{ij}^{LJmin} = \sigma_{ij}$ and $r_{ij}^{LJmax} = 2^{1/6}\sigma_{ij}$ to maximize the width of the switching region while maintaining the minimum of the LJ-potential unperturbed and taking care that the lower limit does not create artificial reaction barriers. The choice of $r_{ij}^{LJmin} = \sigma_{ij}$ also keeps the second derivative of the functional continuous.

The other criterion function in Eq. 3.24 is the bonding switch $S\left(t_b\left(\bar{B}_{ij}^*\right)\right)$. Here the argument function $t_b\left(\bar{B}_{ij}^*\right)$ scales the Brenner model bond-order term $\bar{B}_{ij}$ (Eq. 3.10) to be suitable for Eq. 3.26:

$$t_b\left(\bar{B}_{ij}^*\right) = \frac{\bar{B}_{ij}^* - \bar{B}_{ij}^{*min}}{\bar{B}_{ij}^{*max} - \bar{B}_{ij}^{*min}}. \qquad (3.28)$$

In other words, when the bond order is large, $t_b > 1$ and the Lennard-Jones interactions will not be present. On the other hand, if $\bar{B}_{ij}^*$ is small, the LJ term will be present in a degree appropriate to the prevalent covalent bonding strength. To account for the fact that LJ interaction is typically computed between atoms that are further distanced than the covalent interaction cut-off R_{CC}^l, a bond order term $\bar{B}_{ij}^*$ with slight difference to the original bond order term $\bar{B}_{ij}$ presented by Eq. 3.10 is employed:

$$\bar{B}_{ij}^* = \bar{B}_{ij}|_{r_{ij}=r_{ij}^{LJmin}}. \qquad (3.29)$$

The C_{ij} functional criterion of Equation (3.25) cuts off LJ interactions between atoms that are first, second or third neighbors. This decouples the covalent interaction description and the dihedral rotation description from the long-range interactions. The function C_{ij} is a distance based function that smoothly scales from one to zero over the bonding region.

The second modification to the Brenner model, the dihedral correction E_{tors}, is relevant for the description of saturated hydrocarbons. The original Brenner model does not differentiate between rotated configurations of these. Stuart *et al.* add a barrier for rotations by introducing a torsional potential with the physical symmetries and barrier heights thus removing arbitrary rotations present in the original Brenner. The systems described in this thesis are all-carbon and therefore the exact funtional form of the modification is not discussed here. For detailed information, please refer to Ref. [83].

3.2.4 Density functional theory based tight binding

The tight binding method employed in this thesis is the density functional theory (DFT) based method introduced by Prof. Frauenheim and his group [84, 85]. The basic idea of the density functional based tight binding (DFTB) model is to employ a linear combination of atomic orbitals (LCAO) to form the molecular wave function Ψ. The atomic orbitals ϕ_v are expressed by

$$\phi_v(\vec{r}) = \sum_{i=1}^{N_i} \sum_{j=1}^{N_j} a_{n,i,j} r^{l+i-1} e^{-\alpha_j r} Y_{l,m}\left(\frac{\vec{r}}{r}\right),\qquad(3.30)$$

where $\vec{r}$ is the position of an electron and n, l, and m refer to the main and the angular quantum numbers. The factors N_i, N_j and α_j are chosen to yield an accurate basis set.

The coefficients $a_{n,i,j}$ can be obtained by solving the Kohn-Sham equations of single atoms. The Kohn-Sham equations are modified by an artificial contraction potential that redistributes the electron density far from the nuclei but maintains the close-range electron density. The Kohn-Sham equation with this modification reads:

$$\left[-\frac{\hbar^2}{2m_e}\nabla^2 + V^{\text{nuc+ce}} + e^2 \int \frac{n_{\text{ve}}(\vec{r}')}{|\vec{r}-\vec{r}'|}d^3\vec{r}' \right.$$
$$\left. +\frac{\partial\left(n_{\text{ve}}(\vec{r})\epsilon_{\text{hom}}^{\text{xc}}n_{\text{ve}}(\vec{r})\right)}{\partial n_{\text{ve}}(\vec{r})} + \left(\frac{r}{r_0}\right)^2 \right]\phi_v(\vec{r}) = \epsilon_v\phi_v(\vec{r}).\qquad(3.31)$$

where nuc refers to the nuclei, ce to the core electrons, and ve to valence electrons. The term $\epsilon_{\text{hom}}^{\text{xc}}$ is the exchange correlation energy density of a homogenous electron gas with a density n_{ve}, and the equation therefore is in local density approximation (LDA). The first term inside the parenthesis describes the kinetic energy

operator, the second describes the potential energy of the nuclei and the core electrons (pseudopotential approximation), the third term describes the valence electrons and the last term inside the parenthesis is the confinement term. These equations are solved within the DFT and a set of basis functions ϕ_ν are obtained for each atom type.

Now that we have the basis functions, we return to the many body Schrödinger equation. The Hamiltonian matrix elements are obtained by replacing the many body system effective potential V_{eff} by a superposition of the atomic potentials. The effective potential becomes

$$V_{\text{eff}}(\vec{r}) = \sum_m V_0^m(|\vec{r} - \vec{R}_m|) , \qquad (3.32)$$

where $\vec{R}_m$ is the site vector of atom m. The constituting neutral potentials V_0^m read

$$V_0^m(r) = V^{\text{nuc+ce}} + \text{e}^2 \int \frac{n_{\text{ve,c}}^m(\vec{r}')}{|\vec{r} - \vec{r}'|} d^3\vec{r}' + \frac{\partial \left(n_{\text{ve,c}}^m(\vec{r}) \epsilon_{\text{hom}}^{\text{xc}} n_{\text{ve,c}}^m(\vec{r}) \right)}{\partial n_{\text{ve,c}}^m(\vec{r})} , \qquad (3.33)$$

where $n_{\text{ve,c}}^m$ is the confined electron density of atom m.

The molecular orbitals can be written as a linear combination of the basis functions

$$\Psi_i(\vec{r}) = \sum_{\nu,m} c_{\nu i} \phi_\nu(\vec{r} - \vec{R}_\alpha) . \qquad (3.34)$$

Next, variational analysis of the secular equations leads to a matrix relation between the coefficients $c_{\nu i}$

$$\sum_\nu^M c_{\nu i} \left(H_{\mu\nu}^0 - \varepsilon_i S_{\mu\nu} \right) , \quad \forall \mu , i , \qquad (3.35)$$

where

$$H_{\mu\nu}^0 = \left\langle \phi_\mu | \hat{H}_0 | \phi_\nu \right\rangle \qquad (3.36)$$

and

$$S_{\mu\nu} = \left\langle \phi_\mu | \phi_\nu \right\rangle . \qquad (3.37)$$

The Hamiltonian matrix elements yield

$$H_{\mu\nu}^0 = \begin{cases} \varepsilon_\mu^{\text{neutral free atom}} & \text{if } \mu = \nu, m = n \\ \left\langle \phi_\mu^\alpha \left| \hat{T} + V_0^m + V_0^n \right| \phi_\nu^\beta \right\rangle & \text{if } m \neq n \\ 0 & n = m , \mu \neq \nu. \end{cases} \qquad (3.38)$$

Here the indices m and n refer to the atom around which the wave functions are centered on and μ and ν to the basis orbitals.

The total energy within the DFTB method is written

$$E_{\text{tot}} = \sum_i \int \epsilon_{i,k} d\vec{k} + E_{\text{rep}},$$

(3.39)

where the integration is over the k space and the repulsive contribution can be obtained by taking the difference of the self consistent field DFT cohesive energy and the corresponding TB band structure energy:

$$E_{\text{rep}}(R) = \left\{ E_{LDA}^{SCF} - \sum_i \int \epsilon_{i,k} d\vec{k} \right\} \Bigg|_{\text{reference structure}}$$

(3.40)

The forces resulting from the energy expression 3.39 can be calculated as described in Section 3.2.1 where molecular dynamics is dealt with.

Chapter 4

Overview of the results

This thesis consists of two parts. In the first part the attention is on perfect nanotube structures under strain and the resulting deformations, defects and stability. This research is covered by Publications I-III. Publications IV-VI, the second part of the thesis, address the properties of nanotubes with defects. In them the question whether defects can be employed to improve the mechanical properties of a nanotube sample is addressed. The work describes defect induced roughening of the nanotube surface, *i.e.*, mechanical load transfer through common defects. The mechanical degradation of the properties of individual nanotubes when the defects are present is also assessed.

4.1   Nanotubes under strain: toroidal and bent nanotube structures

Publications I and II were motivated by the experimental observations of μm-sized toroidal nanotubes [15, 16]. The reason is that closed nanotube rings should have interesting electronic and magnetic properties [105–108]. Besides this, a nanotube circle is a uniformly bent nanotube. Nanotubes can be under bending strain, for example, because of pinning to the substrate or because of mechanical loading or manipulation. The uniform bending strain induces changes in the structure and stability that have been assessed in Publications I and II.

In Publication I large toroidal carbon nanotubes were studied using molecular dynamics simulations and the Brenner interaction model [82]. We examined nanotori with diameters in the size range between 22 nm and 700 nm. For the largest tori, that is, tori in the experimentally observed [15, 16] size regime, the curvature does not cause significant structural changes in the cross-section or distribution of atoms. For tori that are considerably smaller than the experimentally observed ones the cross-section was found to deform into an ellipse. If the amount of local curvature exceeded a critical curvature radius, the torus was
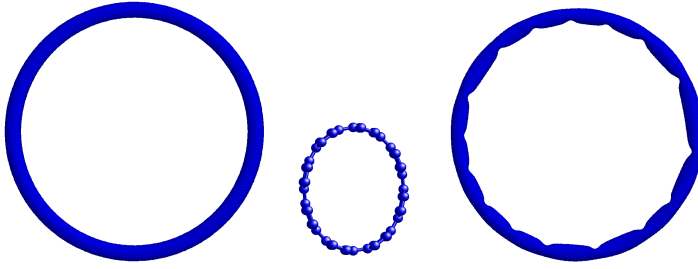
Figure 4.1: Examples of strain-induced deformations in nanotubes. The structure on the left maintains its circular symmetry although the cross-section deforms into an ellipse (center image). The structure on the right has buckled because the local curvature has exceeded a critical value. Publications I and II address questions related to the toroidal structures.

found to buckle. Relatively high diffusion barriers prevent the formation of defects and the observed buckling does not change the hexagonal bonding configuration although the bonding angles deformed to account for the buckles. Figure 4.1 shows examples of strain-induced deformations in nanotubes.

The results of Publication I can be extended to bent nanotubes, because such structures often are under similar local strain conditions as the toroidal structures. Experimental observations of nanotube bends [48, 109] seem to show similar buckling behavior as we report here. Nanotori with (n, n)-chirality, that is, armchair tubes, seemed to have smaller critical buckling radii than the corresponding tori formed of $(n, 0)$-tubes, or zigzag tubes. Details of the index-based structural classification of the nanotubes can be found at Appendix A. Deformations that include buckling induce more drastic changes in the conductivity properties than an elliptical deformation of the nanotube cross-section [26, 27, 110].

Publication II extends the discussion of toroidal nanostructures to the thermal stability of the structures and to comparison with nonuniform bending. The structures are found to be thermally extremely stable and to hold their form at highly elevated temperatures. For tori of the experimentally observed sizes, the diameter of the tube was found to be a much more significant factor for the stability than the toroidal form. The barriers for defect formation were observed to be extremely high: Thermal treatment by high temperature was required to induce defects, for example pentagon–heptagon defect pairs. The results considering the thermal stability of the nanotori indicate that much smaller stable toroidal structures than the circles observed in Refs. [15, 16] can exist. If the means of synthesizing tiny nanotori can be developed, the rings would have applications in nanoelectronics.

When comparing the uniform toroidal bending behavior with dynamical bending at finite temperature we observed buckling for sufficiently large local curvature, buckle propagation, plastic defect formation and fracture depending on the local

strain in the structure. Due to simulations based restrictions on timescales the bent structure is at a non-equilibrium state. The behavior in dynamical bending seems to be locally similar in many ways to the behaviour found in toroidal structures. It should be noted that the bending configurations are far from equilibrium which may affect the description accuracy of the interatomic model potential used in this work.

Publication III presents further work related to structural properties of nanotubes under bending conditions. Besides the classical molecular dynamics model with an empirical interaction potential by Brenner [82], a tight binding model by Frauenheim *et al.* [84, 85] was employed. Unlike in the toroidal case of Publication I, the dynamically bent nanotubes in Publication III do not show significant chirality dependence on the onset of buckling, which may be due to somewhat different conditions, *i.e.*, the study is dynamical and performed at a finite temperature. The present approach with finite temperature is likely to muffle the chirality dependence observed in the more static study of Publication I.

Tight binding simulations predict different location for buckling to appear and a larger amount of deformation in the tube. In addition significantly more conversion from sp^2-bonding to sp^3-bonding is observed than in the simulations based on the Brenner model. The agreement with the classical method is better for small bending angles and for small distortions. However, the greater resistance of the Brenner potential model to switch to sp^3 bonding should be taken into account when interpreting the results of strongly bent structures.

We reported that although the models predict similar behavior when the nanotube structure is only slightly deformed, the results differ significantly when buckling occurs. Our conclusion is that although qualitatively the tight binding and the empirical models predict similar behavior, the latter is not sufficient if exact structural information of the deformations is required.

4.2 Mechanical properties of defective nanotubes

As discussed in Section 2.3.2, the surfaces of pristine nanotubes slide extremely easy with respect to each other. The low-friction behavior enables many nanoelectromechanical applications but it can also be an undesired property. For example, if nanotubes are employed as reinforcement agents, an improved load transfer to the surroundings may be desirable. The strength of mechanical contact between two nanotubes also affects the sample properties, for example, bundles of nanotubes bend and split easily. The following results aim at assessing whether defects can be employed to improve the mechanical properties of a nanotube sample in terms of the load transfer.

In Publication IV the static friction force between the shells of a MWNT, that is, the force required to depin a shell of a MWNT, was assessed first by a
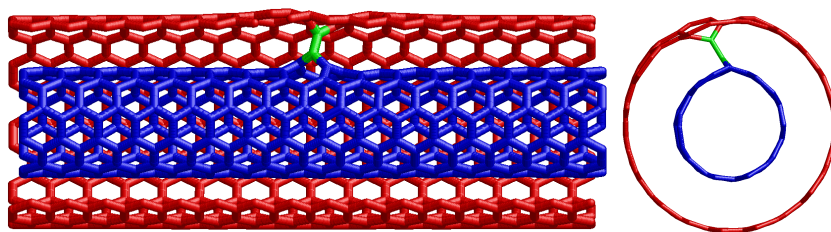
Figure 4.2: An example of a covalent intershell bond formed by two vacancies in adjanced nanotube layers. Publication IV reports that such bonds transfer mechanical load efficiently between nanotubes.

qualitative analysis of the situation and then by quantitative molecular dynamics simulations. In order to do so we employed the Stuart potential energy model [83]. The analytical analysis indicated that the static friction force had three main contributions. The first component of the force results from the capillary force that is due to the change in the overlapping surface area when a shell of a MWNT is pulled out. The capillary force scales with the tube diameter. The second significant contribution is due to the interacting surfaces and can be called the shear term. It scales with the interaction area. The remaining contribution to the static friction force is due to defects and imperfections in the tubes and scales with the pinning strength and density of the defects.

For defect-free nanotubes the capillary contribution dominates the onset of sliding when the tubes are short. For long tubes the force scales with the interaction area because the shear term dominates. We calculated the cross-over length to be approximately 300 nm. If the shells of a MWNT are not perfect, the defects induce an additional contribution to the pinning force. We evaluated this contribution by assessing the pinning strength of defects typical to irradiation. Irradition-induced defects were considered because we proposed irradiation as an efficient means of inducing defects.

We found that the typical values of the force needed to depin the shells in a short double-walled carbon nanotube (DWNT) with a vacancy in the inner tube are typically 0.1 nN−0.4 nN. Correspondingly a single defect compound that results in a covalent bond between the tubes pins the layers with a force of 4 nN−8 nN. Figure 4.2 shows an example of such defect compound. The values corresponding to covalent bonding are of the same order of magnitude as the capillary force, but much larger than the shear forces in short nanotubes. This means that for an MWNT with a diameter of about 6 nm and length of $\sim$ 500 nm, the onset of sliding is governed not by frictional forces resulting from the inter-shell interaction energy corrugation, but by the defects even if there are only 1–2 such defects in the sliding shells. This corresponds to a defect concentration of $\sim$ 10^{-6} Å^{-2} in the sliding shells, that is, a linear concentration

of 1 defect per 300 nm, or a volume concentration of $\sim 5 \cdot 10^{17}$ cm^{-3}. For defects that do not bond the shells covalently the corresponding value is a defect concentration of $\sim 10^{-5}$ Å^{-2} (linear concentration of 1 defect per 10 nm, and volume concentration of $\sim 2 \cdot 10^{19}$ cm^{-3}). The load transfer effect of non-covalent bonds appears smaller than that of covalent bonds but it should be noted that inter-shell links have a lower probability to be formed. Nevertheless, already a few of them have a significant effect on the load transfer.

By irradiating the MWNT with energetic electrons or ions one can easily create a substantial amount of defects in the MWNT – even up to the complete amorphization and collapse of the tube [66]. Thus, although sliding should occur between the shells with the lowest defect concentration, the irradiation dose needed for pinning the shells can be achieved. Notice that neutron irradiation of graphite, which should also result in links between planes, gives rise to a growth in shear modulus with an increase in irradiation dose [111]. Since the mechanism of defect formation should be the same, these experimental results support the predictions of Publication IV.

Inevitably high doses will also result in the deterioration of mechanical characteristics of the nanotube [112]. However, the results of Publication V show that the small amount of defects (a linear concentration of 1 defect per 10 nm, or per 300 nm if the defects involve covalent inter-shell links) that is required to transfer the axial mechanical load from one of the sliding shells to the other, will affect only slightly the nanotube Young's modulus and critical strength. Thereby, using, *e.g.*, the transmission electron microscope (TEM) with electron energies higher than the the minimum energy of the electron required to knock a carbon atom out of its original position (~ 100 keV [113]), one can prevent the shell sliding and thus partially transfer the mechanical load from one of the shells to the other. Note that the irradiation can be used in a similar fashion to transfer load from the SWNTs at the perimeter of a SWNT rope to the inner tubes. TEM was employed in experiments [55–58] on MWNT telescopic properties to monitor the motion of the shells — the same setup can immediately be applied to testing of how the load is transferred between the shells (given that the electron beam energy is higher than the threshold). Such an experiment should also be interesting in elucidating the behavior of irradiation-induced defects in nanotubes and graphite.

We proposed a scheme for employing irradiation to weld together nanotube shells selectively based on the energy, and thus the penetration depth, of the incident particle [77]. Because the electron energy threshold for displacing carbon atoms should be slightly lower for nanotubes with smaller diameters due to curvature effects which generate some strain in the carbon network, the electrons with energies just above the threshold should create damage mainly in the inner shells. This, combined with atomic force microscope manipulation of the tubes, opens up new techniques for nanoengineering. Due to much larger ranges and smoother defect distribution, only electron irradiation can be used for transferring

the load between the shells in MWNTs in macroscopic samples, *e.g.*, MWNT-based composite materials.

To conclude, in Publication IV the results of a molecular dynamics study of the telescopic behavior of MWNTs and conditions for the effective load transfer between shells of MWNTs were reported. We simulated the response of pristine MWNTs and nanotubes with irradiation-induced defects to the external force acting on one of the shells. In addition, we demonstrated that a small amount of defects can increase the interlayer shear strength by several orders of magnitude and, thus, small-dose electron or ion irradiation can be employed for the mechanical load transfer between the shells. Finally we discussed how the experimental setup used in previous studies on MWNT telescopic behavior can be employed for checking our results and improving our understanding of irradiation-induced phenomena in graphitic materials.

Publication V reports the results of a theoretical study that assesses the effects of vacancy-related defects on the mechanical characteristics of single-walled carbon nanotubes. Figure 4.3 shows examples of the studied defects. Vacancies can be expected to degrade the mechanical strength because nanotubes are essentially one dimensional in structure. Therefore, any deficiencies in the atomic network should affect the strength significantly and thus possibly vitiate the benefits reported in Publication IV. The results of Publication V indicate that although individual tubes degrade mechanically, defects can be considered as means to transfer load between nanotubes. Specifically, in Publication V we calculated the Young's modulus and tensile strength of SWNTs with vacancies for different defect concentrations and vacancy types. These were first assessed by continuum theory based analytics and then classical molecular dynamics simulations employing the Brenner interaction model.

We reported that the Young's modulus of the nanotubes depends weakly on the vacancy concentration: a relatively high defect density of one vacancy per 50 Å gives rise to a small decrease in the Young's modulus: only about 3 %, if we consider a thin $(5, 5)$ nanotube. Thin tubes are most sensitive to defects and therefore the effect is even less if the tube has a larger diameter. Vacancy reconstructions by saturating dangling bonds were reported to diminish the degradation for the majority of the tubes and vacancy orientations studied.

We also showed that vacancies have a much stronger effect on the tensile strength of nanotubes. The work done in Publication V indicates that the tensile strength can degrade down to 60 % of the intact tube value if even a single vacancy is present. For the critical strain the effect can be even more deleterious. The critical strain of the defective SWNT can be half of the intact tube value. Similar to the nanotube Young's modulus, the degradation of tensile characteristics is partly alleviated by the ability of the nanotube carbon network to heal the vacancy damage by saturating the dangling bonds. However, even reconstructed defects decrease the tensile characteristics by 5 % − 10 % for the zig-zag tubes and
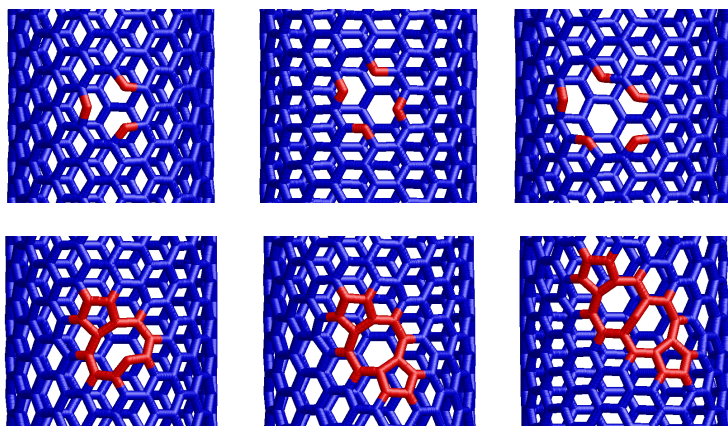
Figure 4.3: A (10, 10)-nanotube with single and multiple vacancies. The images below show the structure when the nanotube has been thermally annealed to heal the atomic network. Publication V addresses the mechanical degradation of individual nanotubes due to such defects.

$10\,\% - 15\,\%$ (tensile strength) and $25\,\% - 30\,\%$ (critical strain) for the armchair tubes. Overall, the tensile characteristics, especially if defects were present, were observed to be chirality dependent. This is consistent with the previous reports on tensile strength dependence on chirality for intact tubes [43].

The results of Publication V indicate that the Young's modulus of nanotubes with defects will essentially be the same unless the vacancy concentration is extremely high. On the other hand, the tensile strength will substantially drop due to the quasi-one-dimensional atomic structure of SWNTs already if a single vacancy is present – the tensile strength of a SWNT is governed by the "weakest" segment of the tube. Given that a small number of defects are always present in nanotubes, this may explain why the theoretically predicted Young's modulus agrees well with the experimentally measured values, while the tensile characteristics are much worse.

Finally, within the framework of the continuum theory we have derived an expression which can be used to calculate the Young's modulus of defective CNTs at an arbitrary vacancy concentration, unless the defect concentration is so high that there are several defects in a specific unit cell of the nanotube. Thus, knowing the irradiation dose and defect production rate one can evaluate the drop in Young's modulus, which is indispensable for the qualitative explanation of the recent experimental data on the behavior of Young's modulus of irradiated nanotube bundles [79]. Note also that the defect concentration and ideally the defect types can be estimated by probing the electronic structure of nanotubes by using various experimental techniques such as Raman, electron spin resonance and optical absorption spectroscopy. Thus, simultaneous monitoring of the nanotube
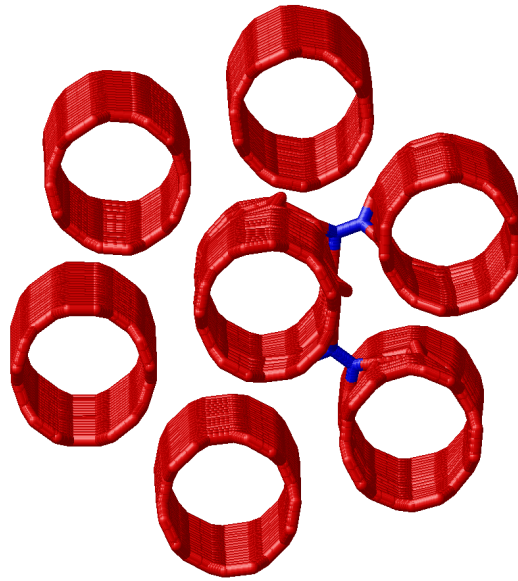
Figure 4.4: A section of a nanotube bundle with defect-induced links. Irradiation-induced structural damage is reported in Publication VI to induce stiffening of nanotube bundles at moderate doses. At high doses the structural weakening overcomes the stiffening effect in accordance to Ref. [79].

mechanical properties and defect concentration can shed light on the properties of irradiation-induced defects in carbon nanotubes.

Publication VI extends the discussion of defect mediated load transfer in MWNTs to bundles of single walled nanotubes. Electron irradiation measurements in Ref. [79] showed a dramatic increase of the bending stiffness of a nanotube bundle at moderate irradiation doses and then followed by a mechanical degradation at higher doses. This is highly relevant in nanotube–polymer composites in which the bundle acts as reinforcement. In Publication VI we present theoretical background for what happens when the nanotube bundle is irradiated. We present analytical formulae based on approximation for electron irradiation damage in nanotubes and we relate this information to the bending stiffness of the bundle. We show that a trade-off between bundle stiffening due to inter-tube covalent bonds and a drop in Young's modulus of the individual nanotubes due to the irradiation induced defects can explain the steeply increasing and then decreasing bending modulus value observed in electron irradiation measurements in Ref. [79]. The studied system is presented in Figure 4.4. Based on the results we can draw the conclusion that irradiation is a good tool to enhance the mechanical properties of nanotube bundles when they are used as reinforcement agents.

Chapter 5

Summary

In this thesis strained and defective carbon nanotubes were studied by analytical and molecular dynamics simulation methods. The thesis consists of two parts. In the first part of the thesis nanotubes under strain, and in particular under bending strain, were considered. Strain induced deformations and changes in the nanotube structure were assessed. A critical limit in the local curvature was found at which it became energetically favorable for the structures to buckle. Thermal stability was observed to be extremely high and defect formation barriers prevented the formation of structural defects except at very high temperatures.

The observations in the first part of the thesis indicate that toroidal nanotubes with diameters much smaller than the experimentally observed μm sized rings can exist. If such small nanorings can be synthesized, they will have applications in electronics. Based on quantum interference effects the rings show, for example, peculiar localized electron states, colossal paramagnetic moments, persistent currents and exceptional response to external electromagnetic fields. Furthermore, the results of bent structures and the observed high defect formation barriers show how remarkably flexible and strong the nanotubes are.

In the second part of the thesis the use of defects as a means to improve mechanical contact between nanotubes was evaluated. The emphasis was on irradiation-induced defects because irradiation has been proposed as an efficient method of inducing defects in a controlled fashion. Irradiation-induced defects were found to significantly improve load transfer between nanotube shells in multi-walled nanotubes and between tubes in bundles. Already at very low concentrations the defects are the dominating factor in the static friction force between two nanotubes. However, defects inevitably diminish the mechanical strength of individual tubes in the sample. Depending on the magnitude of this effect, the degradation could render the defect-induced increase in load transfer useless for the improvement of the over-all mechanical characteristics of the sample. Therefore, the magnitude of the degradation was assessed. The Young's modulus of the

tubes was found to be insensitive to point defects but the tensile strength decreased significantly even if a single defect was present. The defective nanotubes, even though weakened, were still extremely strong. We reached the conclusion that the improvement in load transfer to the surroundings overcomes the weakening effect and defects can be employed to improve the over-all characteristics of a sample that contains nanotubes. Evidence for this was provided by addressing the bending stiffness of a nanotube bundle in the presence of defects. At moderate irradiation doses and defect densities the bending stiffness shows a dramatic increase but if the defect concentration is extremely high, the weakening in the individual tubes overcomes the effect of increased shear.

The second part shows that defects are not always undesirable in a nanotube structure. They can be used to tailor and to improve mechanical characteristics of a nanotube sample. The results can guide and help in the development of applications where the slippage of nanotubes with respect to each other or the surroundings could be detrimental.

Appendix A

Classification of nanotube structures

The most commonly used notation to differentiate between nanotubes is introduced here. The notation follows that of Ref. [5]. The hexagonal network of Figure A.1 depicts a graphene layer – each of the hexagon corners represents a position of a carbon atom. The graphene layer can be thought as a tube cut open. Therefore the figure can be used to visualize the notation and concepts discussed. The notation of Figure A.1 corresponds to rolling the graphene layer to a tube in such a way that $\vec{OB}$ and $\vec{AB'}$ lie on top of each other.

To begin with, two base vectors $\vec{a}_1$ and $\vec{a}_2$ are defined as shown in Figure A.1. The chiral vector $\vec{C}$ that joins two equivalent points O and A (or equivalently B and B') on the tube surface is

$$\vec{C} = n\vec{a}_1 + m\vec{a}_2 \,. \tag{A.1}$$

Each pair of integers (n, m) represents a possible tube structure and can be used to classify the structures. There exist two possible high symmetry structures for nanotubes known as the zigzag, $(n, 0)$, and the armchair, (n, n). The names derive from the pattern formed when a particular tube is cut perpendicular to the axis. All other combinations of n and m are known as chiral nanotubes. Examples of arm-chair, zig-zag and chiral nanotubes are presented in Fig. A.2. From here on a nanotube structure will be identified by the indices n and m and, correspondingly, it will be referred to as an (n, m)-nanotube [6].

In Figure A.1 it can be seen that the circumference length of the nanotube is the length of the chiral vector, which is given by

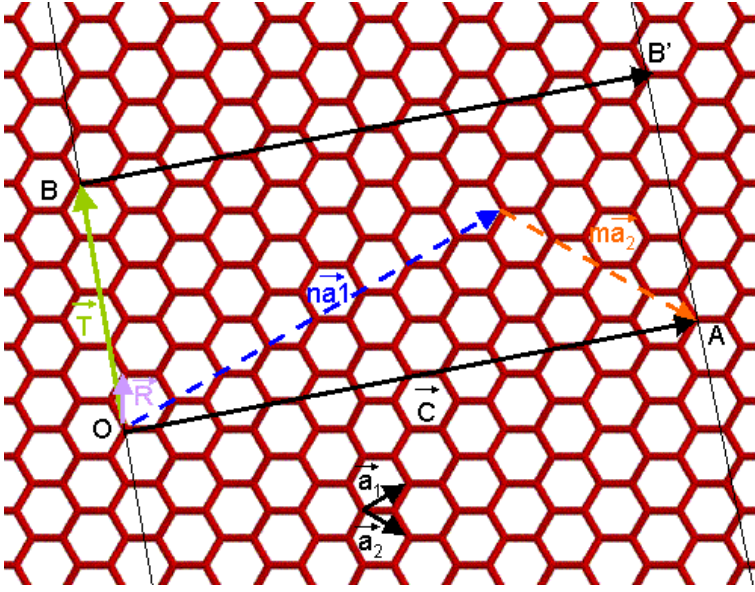$$C = \sqrt{\vec{C} \cdot \vec{C}} = a\sqrt{n^2 + m^2 + nm}, \tag{A.2}$$

Figure A.1: Wrapping a graphite sheet to an (n, m)-nanotube.

where the values

$$\begin{cases} \vec{a}_1 \cdot \vec{a}_1 = \vec{a}_2 \cdot \vec{a}_2 = a^2 \\ \vec{a}_1 \cdot \vec{a}_2 = \frac{a^2}{2} \end{cases} \tag{A.3}$$

have been used for the inner products of $\vec{a}_1$ and $\vec{a}_2$. The graphite lattice constant value can be employed as a first approximation for the length of the base vector

$$|\vec{a}_1| = |\vec{a}_2| = a = 0.24612 \text{ nm}, \tag{A.4}$$

although in nanotubes the curvature induces small chirality dependent variations from graphite bond lengths. Besides the chiral vector, another commonly used term in the study of nanotubes is the chiral angle θ. It is defined as the angle between the vectors $\vec{C}$ and $\vec{a}_1$ and has values ranging from 0 to $\frac{\pi}{6}$ because of the hexagonal symmetry of the graphene lattice. The cosine of the chiral angle is expressed with n and m as

$$\cos \theta = \frac{\vec{C} \cdot \vec{a}_1}{|\vec{C}||\vec{a}_1|} = \frac{n + \frac{m}{2}}{\sqrt{n^2 + m^2 + nm}}. \tag{A.5}$$

A unit cell of a carbon nanotube is defined with the help of the translational vector

$$\vec{T} = t_1 \vec{a}_1 + t_2 \vec{a}_2. \tag{A.6}$$

The vector is normal to the chiral vector and thus parallel to the nanotube axis. It represents the translation required in the direction of the nanotube axis to reach
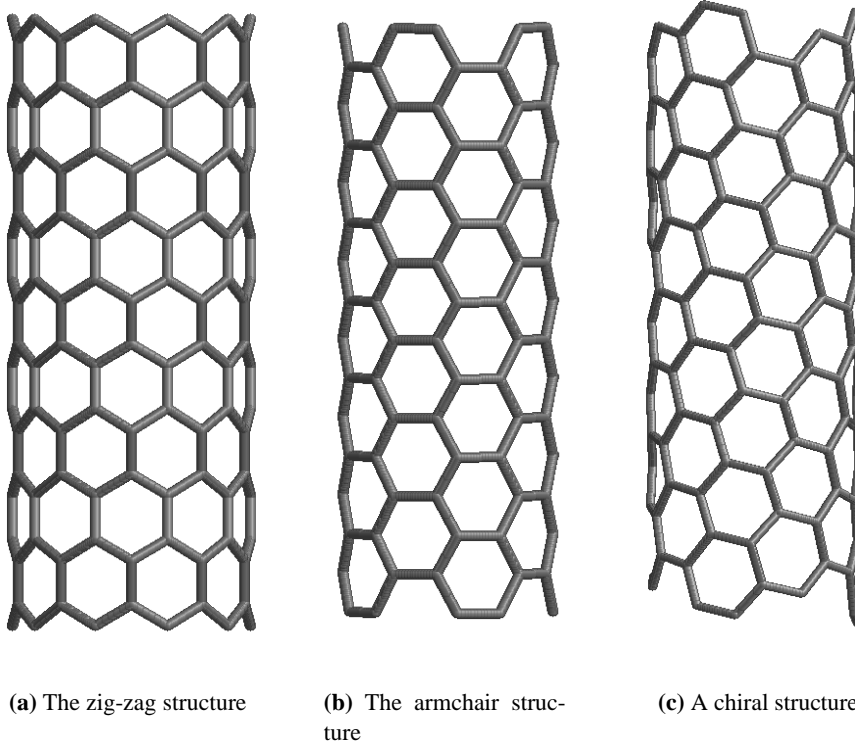
(a) The zig-zag structure   **(b)** The armchair struc-   **(c)** A chiral structure
ture

Figure A.2: Zigzag and armchair structures and an example of a chiral nanotube. The figures present a $(10, 0)$-, a $(5, 5)$- and a $(7, 3)$-nanotube.

the nearest equivalent lattice point. Using the information that $\vec{T}$ is perpendicular to $\vec{C}$, *i.e.*, $\vec{T} \cdot \vec{C} = 0$, expressions for t_1 and t_2 in terms of n and m are obtained:

$$\begin{cases} t_1 = & +A \, (2m + n) \\ t_2 = & -A \, (2n + m) \; . \end{cases} \tag{A.7}$$

The constant A is determined by the requirement that $\vec{T}$ specifies the translation to the nearest equivalent lattice point, that is, t_1 and t_2 do not have a common divisor except unity. Thus

$$A = \frac{1}{\gcd(2m + n, \, 2n + m)} \; , \tag{A.8}$$

where gcd stands for the greatest common divisor of the arguments. The expres-

sions for t_1 and t_2 become

$$
\begin{cases}
t_1 = & \frac{2m+n}{\gcd(2m+n,2n+m)} \\
t_2 = & -\frac{2n+m}{\gcd(2m+n,2n+m)} \,.
\end{cases}
\tag{A.9}
$$

Therefore the unitcell length is is

$$
\begin{aligned}
T =& a\sqrt{t_1^2 + t_2^2 + t_1 t_2} \\
=& \frac{\sqrt{3}C}{\gcd(2m+n, 2n+m)} \,,
\end{aligned}
\tag{A.10}
$$

where Equation (A.2) has been used. The vectors $\vec{C}$ and $\vec{T}$ specify the parallelogram that forms the unit cell of a nanotube. In Figure A.1 the unit cell is the parallelogram $OAB'B$.

The number of atoms in a nanotube unit cell N can be computed by noticing that for each hexagon present there are two atoms in the unit cell. The area of a hexagon is $\frac{\sqrt{3}}{2}a^2$. The number of atoms can be calculated by dividing the area of the unit cell by the area of one hexagon and multiplying the result by the two atoms in each hexagon:

$$
N = \frac{4C^2}{a^2 \gcd(2m+n, 2n+m)} \,.
\tag{A.11}
$$

Now the unit cell of an arbitrary nanotube and the amount of particles are known. There still remains to be explained the way the positions of each atom in the unit cell are computed. To accomplish this, a third vector, the symmetry vector $\vec{R}$, is defined. It is defined as the site vector having the smallest positive component in the direction of $\vec{C}$. In terms of the vectors $\vec{a}_1$ and $\vec{a}_2$ the vector $\vec{R}$ is expressed as

$$
\vec{R} = p\vec{a}_1 + q\vec{a}_2 \,,
\tag{A.12}
$$

where p and q are integers and do not have a common divisor except for unity. The symmetry vector can be used to calculate the site vector of each hexagon in the unit cell

$$
\vec{R}_i = i\vec{R} \,,
\tag{A.13}
$$

where i is the index of each hexagon ($i \in [1, \frac{N}{2}]$). The site vector $\vec{R}_i$ exists only in the unit cell and thus appropriate shifts that keep the vector inside the unit cell must be performed in order to compute the positions of the hexagons correctly [5].

For each hexagon i there exists two atoms. The first one shares the site vector of the hexagons obtained from Equation (A.13) and the other is dislocated by a vector that corresponds to a translation along an edge of the hexagon to the next
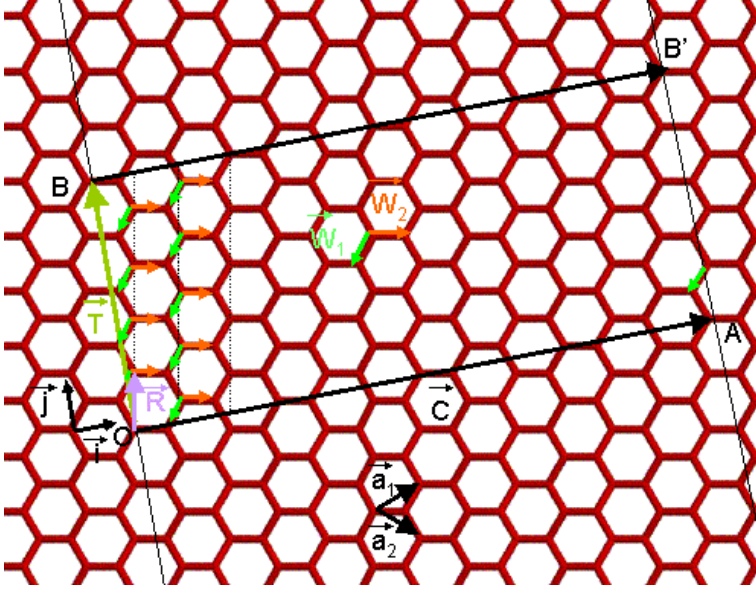
Figure A.3: Calculating the positions of the atoms on the hexagonal network.

site (see Figure A.3). The translation along an edge of the hexagon corresponds to either of the translations

$$
\begin{cases}
\vec{W}_1 = -\frac{2}{3}\vec{a}_1 + \frac{1}{3}\vec{a}_2 \\
\vec{W}_2 = \frac{1}{3}\vec{a}_1 + \frac{1}{3}\vec{a}_2
\end{cases}
\tag{A.14}
$$

depending on which one is chosen. The atom sites can thus be computed using the expressions

$$
\begin{cases}
\vec{R}_i = & i\,\vec{R} \\
\vec{R}_{i+\frac{N}{2}} = & i\left(\vec{R} + \vec{W}_j\right),
\end{cases}
\tag{A.15}
$$

in which $i \in [1, \frac{N}{2}]$. As can be seen in Figure A.3, appropriate shifts must be performed to ensure that the sites are situated inside the unit cell.

So far we have worked in the coordinate system of Figure A.1 and used the vectors $\vec{a}_1$ and $\vec{a}_1$ as the base. Now we move to the coordinate system of a nanotube. The base of the coordinate system is transformed so that the unit vectors in the direction of $\vec{C}$ and and $\vec{T}$ form the new base. Since $\vec{C}$ and $\vec{T}$ are perpendicular, it is natural to choose the Cartesian unit vectors $\vec{i}$ and $\vec{j}$ as the base vectors. The coordinate system is set so that $\vec{i}$ is parallel to $\vec{C}$ and $\vec{j}$ to $\vec{T}$. The graphite lattice constant a is chosen to be the unit distance in the system. In this

base the vectors $\vec{a}_1$ and $\vec{a}_2$ are expressed as

$$
\begin{aligned}
\vec{a}_1 &= \cos(\theta)\,\vec{i} + \sin(\theta)\,\vec{j} \\
\vec{a}_2 &= \cos\left(\frac{\pi}{3} - \theta\right)\vec{i} - \sin\left(\frac{\pi}{3} - \theta\right)\vec{j} \\
&= \frac{1}{2}\left(\cos(\theta) + \sqrt{3}\sin(\theta)\right)\vec{i} + \frac{1}{2}\left(-\sqrt{3}\cos(\theta) + \sin(\theta)\right)\vec{j}.
\end{aligned}
\tag{A.16}
$$

The site of each atom is obtained as

$$
\begin{aligned}
\vec{R}_i &= i\left(\frac{R_C}{a}\vec{i} + \frac{R_T}{a}\vec{j}\right) \\
\vec{R}_{i+\frac{N}{2}} &= i\left(\frac{R_C}{a}\vec{i} + \frac{R_T}{a}\vec{j} + \vec{W}_j\right),
\end{aligned}
\tag{A.17}
$$

where $i \in [1, \frac{N}{2}]$, R_C is the component of $\vec{R}$ on $\vec{C}$, and R_T is the component of $\vec{R}$ on $\vec{T}$. Again, appropriate shifts to keep the site vectors inside the unit cell must be performed. The projections R_C and R_T are

$$
\begin{aligned}
R_C &= \frac{\vec{C} \cdot \vec{R}}{|\vec{C}|} = \frac{(2n+m)\,p + (2m+n)}{2C}a^2 \\
&= \frac{t_1 q - t_2 p}{2C}\gcd(2m+n, 2n+m)a^2 \\
R_T &= \frac{\vec{T} \cdot \vec{R}}{|\vec{T}|} = \frac{\sqrt{3}\,(mp - nq)\,a^2}{4C} \\
&= (mp - nq)\,\frac{T}{N}.
\end{aligned}
\tag{A.18}
$$

Introducing Equation (A.16) to the Equations (A.14) the shifts become

$$
\begin{cases}
\vec{W}_1 = \frac{1}{2}\left(-\cos(\theta) + \frac{1}{\sqrt{3}}\sin(\theta)\right)\vec{i} - \frac{1}{2}\left(\sin(\theta) + \frac{1}{\sqrt{3}}\cos(\theta)\right)\vec{j} \\
\vec{W}_2 = \frac{1}{2}\left(+\cos(\theta) + \frac{1}{\sqrt{3}}\sin(\theta)\right)\vec{i} + \frac{1}{2}\left(\sin(\theta) - \frac{1}{\sqrt{3}}\cos(\theta)\right)\vec{j}.
\end{cases}
\tag{A.19}
$$

If the values of the coefficients p and q are known, the Equations (A.17) - (A.19) can be used to calculate the site vectors of each particle. Let us now determine the values of p and q. To begin with the symmetry vector $\vec{R}$ exists inside the unit cell: its projections on the vectors $\vec{C}$ and $\vec{T}$ must be shorter than the vectors themselves. Therefore $\vec{R}$ must satisfy

$$
\begin{cases}
0 < \frac{\vec{R} \cdot \vec{T}}{|\vec{T}|^2} = \frac{2(mp - nq)}{N} \leq 1 \\
0 < \frac{\vec{R} \cdot \vec{C}}{|\vec{C}|^2} = \frac{2(2n+m)p + 2(2m+n)q}{N} \leq 1,
\end{cases}
\tag{A.20}
$$

which can be simplified to

$$\begin{cases} 0 < mp - nq \le \frac{N}{2} \\ 0 < (2n + m)\,p + (2m + n)\,q \le \frac{N}{2}\,. \end{cases} \qquad \text{(A.21)}$$

By definition $\vec{R}$ is the site vector that has the smallest positive component on the vector $\vec{C}$. Therefore the projection

$$\begin{aligned} R_C &= \frac{\vec{C} \cdot \vec{R}}{|\vec{C}|} = \frac{(2n + m)\,p + (2m + n)\,q}{2C}a^2 \\ &= \frac{t_1 q - t_2 p}{2C}\gcd(2m + n, 2n + m)a^2 \end{aligned} \qquad \text{(A.22)}$$

must be minimized. Since p, q, n, and m are integers and n and m are positive or zero, the p and the q that give the smallest projection component on vector $\vec{C}$ must satisfy

$$t_1 q - t_2 p = 1\,. \qquad \text{(A.23)}$$

The left side can not be negative or equal to zero because Equation (A.22) must give a positive nonzero value for R_C. Taking into account the constrictions of Equations (A.21), there is only one pair of coefficients that satisfies Equation (A.23). In practice the pair is found by looping through the possibilities allowed by Equations (A.21).

With p and q solved the site vectors of each particle of the unit cell can be calculated. The site vectors obtained are on a plane and a transformation must be performed in order to obtain a cylindrical three dimensional form. The site vector $\vec{R}_i$ of a particle is expressed by its components as

$$\vec{R}_i = x_i \vec{i} + y_i \vec{j} \qquad \text{(A.24)}$$

and while the y_i component is kept intact, the x_i and the z_i components undergo a transformation:

$$\begin{cases} z_i' = \quad + \sin(\frac{x_i}{r_{tube}})r_{tube} \\ x_i' = \quad - \cos(\frac{x_i}{r_{tube}})r_{tube}\,, \end{cases} \qquad \text{(A.25)}$$

where r_{tube} is the radius of the tube and is obtained from

$$r_{tube} = \frac{C}{2\pi}\,. \qquad \text{(A.26)}$$

The coordinates of each atom in an arbitrary nanotube are thus obtained from the expression

$$\begin{aligned} \vec{R}_i' &= x_i' \vec{i} + y_i' \vec{j} + z_i' \vec{k} \\ \vec{R}_i' &= - \cos(\frac{x_i}{r_{tube}})r_{tube}\vec{i} + y_i \vec{j} + \sin(\frac{x_i}{r_{tube}})r_{tube}\vec{k}\,, \end{aligned} \qquad \text{(A.27)}$$

where $\vec{k}$ is the third Cartesian base vector ($\vec{i}$, $\vec{j}$, and $\vec{k}$ form an orthonormal base with a as the unit length), and x_i, and y_i are the coordinates of atoms on the hexagonal plane. As seen in Figure A.2, the tube axis is along the y-axis and the tube cross-section lies on the xz-plane in the coordinates chosen.

The unit cell created the way explained above can be multiplied thus manifolding the resulting tube length. The method presented allows also the use of periodic boundary conditions in the direction of the tube axis, although then only integer multiples of unit cells can be piled on top of each other.

Appendix B

Brenner potential energy model: Calculating the forces

In this appendix computing the interparticle forces according to the Brenner inter-action model [82] is discussed. The force on a particle m is the negative gradient of the potential $\vec{f}_m = -\nabla_m E_b$. In the case of the Brenner model the potential energy E_b for an all-carbon system is given by Equation (3.21). Taking into account the symmetries the force becomes

$$
\begin{aligned}
\vec{f}_m = &-\sum_{j\neq m} \frac{D^{(e)}}{S-1} e^{\sqrt{2S}\beta(R^e - r_{mj})} \left[\sqrt{2S}\beta f_{mj} \frac{\vec{r}_{mj}}{r_{mj}} + \nabla_m f_{mj} \right] \\
&- \sum_{j\neq m} \frac{1}{2}\frac{D^{(e)}S}{S-1} e^{\sqrt{\frac{2}{S}}\beta(R^e - r_{mj})} \left[\delta f_{mj}\left(1 + \sum_{k\neq m,j} G\left(\theta_{mjk}\right) f_{mk}\right)^{-\delta-1} \cdot \right. \\
&\qquad \cdot \sum_{k\neq m,j} \left[f_{mk}\nabla_m G\left(\theta_{mjk}\right) + G\left(\theta_{mjk}\right)\nabla_m f_{mk} \right] \cdot \\
&\qquad \delta f_{mj}\left(1 + \sum_{k\neq m,j} G\left(\theta_{jmk}\right) f_{jk}\right)^{-\delta-1} \cdot \sum_{k\neq m,j} f_{jk}\nabla_m G\left(\theta_{jmk}\right) \\
&\qquad - f_{mj}\nabla_m F_{mj} + \left[\sqrt{\frac{2}{S_{mj}}}\beta f_{mj}\frac{\vec{r}_{mj}}{r_{mj}} - \nabla_m f_{mj}\right] \cdot \\
&\qquad \left. \cdot \left[\left(1 + \sum_{k\neq m,j} G\left(\theta_{mjk}\right) f_{mk}\right)^{-\delta} + \left(1 + \sum_{k\neq m,j} G\left(\theta_{jmk}\right) f_{jk}\right)^{-\delta} + F_{mj}\right]\right] \\
&- \sum_{j\neq m}\sum_{k\neq m,j} \frac{1}{2}\frac{D^{(e)}S}{S-1} e^{\sqrt{\frac{2}{S}}\beta(R^e - r_{kj})} f_{kj} \cdot \left[\left(1 + \sum_{l\neq j,k} G\left(\theta_{kjl}\right) f_{kl}\right)^{-\delta-1} \cdot \right. \\
&\qquad \left. \cdot \left(f_{km}\nabla_m G\left(\theta_{kjm}\right) + G\left(\theta_{kjm}\right)\nabla_m f_{km}\right) - \frac{1}{2}\nabla_m F_{kj}\right].
\end{aligned}
$$

(B.1)

The treatment covers the carbon-only parts of the interaction model. Therefore a shorthand notations for the parameters have been used. δ, $D^{(e)}$, S, and β map to the corresponding hydrocarbon parameters, for example, $\delta = \delta_{CC} = \delta_{ij}$. The hydrogen description is omitted because the research done in this thesis does not cover hydrocarbon structures.

Writing

$$\cos\left(\theta_{ijk}\right) = \frac{\vec{r}_{ij} \cdot \vec{r}_{ik}}{r_{ij} r_{ik}} \tag{B.2}$$

the gradient of the function $G\left(\theta_{ijk}\right)$ of Equation (3.16) becomes

$$\nabla_m G\left(\theta_{ijk}\right) = -\frac{2a_0 c_0^2 \left(1 + \frac{\vec{r}_{ij}\cdot\vec{r}_{ik}}{r_{ij}r_{ik}}\right) \nabla_m \frac{\vec{r}_{ij}\cdot\vec{r}_{ik}}{r_{ij}r_{ik}}}{\left(d_0^2 + \left(1 + \frac{\vec{r}_{ij}\cdot\vec{r}_{ik}}{r_{ij}r_{ik}}\right)^2\right)^2}, \tag{B.3}$$

where the term $\nabla_m \frac{\vec{r}_{ij}\cdot\vec{r}_{ik}}{r_{ij}r_{ik}}$ has the following values depending on whether the indices run jmk, kjm, or mjk:

$$\nabla_m \frac{\vec{r}_{jm}\cdot\vec{r}_{jk}}{r_{jm}r_{jk}} = -\frac{1}{r_{jm}r_{jk}}\left[\vec{r}_{jk} - \left(\frac{\vec{r}_{mj}\cdot\vec{r}_{jk}}{r_{mj}^2}\right)\vec{r}_{mj}\right]$$

$$\nabla_m \frac{\vec{r}_{kj}\cdot\vec{r}_{km}}{r_{kj}r_{km}} = -\frac{1}{r_{mk}r_{kj}}\left[\vec{r}_{kj} - \left(\frac{\vec{r}_{mk}\cdot\vec{r}_{kj}}{r_{mk}^2}\right)\vec{r}_{mk}\right] \tag{B.4}$$

$$\nabla_m \frac{\vec{r}_{mj}\cdot\vec{r}_{mk}}{r_{mj}r_{mk}} = -\frac{1}{r_{jm}r_{mk}}\left[1 + \left(\frac{\vec{r}_{jm}\cdot\vec{r}_{mk}}{r_{jm}^2}\right)\right]\vec{r}_{jm}$$
$$-\frac{1}{r_{jm}r_{mk}}\left[1 - \left(\frac{\vec{r}_{jm}\cdot\vec{r}_{mk}}{r_{mk}^2}\right)\right]\vec{r}_{mk}.$$

Gradients involving index combinations without m are zero.

In order to obtain the gradient of F_{ij} some manipulation of the differentials is required. Using the chain rule [114] $\nabla_m F_{ij}$ can be expressed as

$$\nabla_m F_{ij}\left(N_i^{(t)}, N_j^{(t)}, N_{ij}^{\mathrm{conj}}\right) = \frac{\partial F_{ij}\left(N_i^{(t)}, N_j^{(t)}, N_{ij}^{\mathrm{conj}}\right)}{\partial N_i^{(t)}}\nabla_m N_i^{(t)}$$
$$+ \frac{\partial F_{ij}\left(N_i^{(t)}, N_j^{(t)}, N_{ij}^{\mathrm{conj}}\right)}{\partial N_j^{(t)}}\nabla_m N_j^{(t)} \tag{B.5}$$
$$+ \frac{\partial F_{ij}\left(N_i^{(t)}, N_j^{(t)}, N_{ij}^{\mathrm{conj}}\right)}{\partial N_{ij}^{\mathrm{conj}}}\nabla_m N_{ij}^{\mathrm{conj}}.$$

Noticing that only $\nabla_m F_{mj}$ and $\nabla_m F_{kj}$ are present in Equation (B.1) the above can be

Table B.1: Parameter values for Brenner's potential energy model.

Parameter	Value	Value
	1ˢᵗ parametrization	2ⁿᵈ parametrization
$R_{CC}^{(e)}$	$1.315 \cdot 10^{-10}$ m	$1.39 \cdot 10^{-10}$ m
$D_{CC}^{(e)}$	6.325eV	6.0 eV
β_{CC}	$1.5 \cdot 10^{10} \frac{1}{m}$	$2.1 \cdot 10^{10}$ 1/m
S_{CC}	1.29	1.22
δ_{CC}	0.80469	0.5
α_{CCC}	0.0	0.0
$R_{CC}^{(1)}$	$1.7 \cdot 10^{-10}$m	$1.7 \cdot 10^{-10}$
$R_{CC}^{(2)}$	$2.0 \cdot 10^{-10}$m	$2.0 \cdot 10^{-10}$
a_0	0.011304	0.00020813
c_0	19	330
d_0	2.5	3.5

simplified to

$$
\begin{aligned}
\nabla_m F_{mj} =& \frac{\partial F_{mj}}{\partial N_m^{(t)}} \nabla_m \left(\sum_k f_{mk} \right) + \frac{\partial F_{mj}}{\partial N_j^{(t)}} \nabla_m \left(\sum_k f_{kj} \right) \\
&+ \frac{\partial F_{mj}}{\partial N_{mj}^{\text{conj}}} \nabla_m \left(\sum_{k \neq m,j} \left[f_{mk} F\left(x_{mk}\right) + f_{jk} F\left(x_{jk}\right) \right] \right) \\
=& \frac{\partial F_{mj}}{\partial N_m^{(t)}} \sum_k \nabla_m f_{mk} + \frac{\partial F_{mj}}{\partial N_j^{(t)}} \nabla_m f_{mj} \\
&+ \frac{\partial F_{mj}}{\partial N_{mj}^{\text{conj}}} \sum_{k \neq m,j} \left(F\left(x_{mk}\right) \nabla_m f_{mk} + f_{jk} \frac{\partial F\left(x_{jk}\right)}{\partial x_{jk}} \nabla_m f_{mj} \right) \\
\nabla_m F_{kj} =& \frac{\partial F_{kj}}{\partial N_i^{(t)}} \nabla_m \left(\sum_j f_{kj} \right) + \frac{\partial F_{kj}}{\partial N_j^{(t)}} \nabla_m \left(\sum_i f_{ki} \right) \\
&+ \frac{\partial F_{kj}}{\partial N_{kj}^{\text{conj}}} \nabla_m \left(\sum_{i \neq k,j} \left[f_{ik} F\left(x_{ki}\right) + f_{ij} F\left(x_{ji}\right) \right] \right) \\
=& \frac{\partial F_{kj}}{\partial N_i^{(t)}} \nabla_m f_{mk} + \frac{\partial F_{kj}}{\partial N_j^{(t)}} \nabla_m f_{mk} \\
&+ \frac{\partial F_{kj}}{\partial N_{kj}^{\text{conj}}} \left(F\left(x_{km}\right) \nabla_m f_{mk} + F\left(x_{jm}\right) \nabla_m f_{mj} \right) \\
&\sum_{i \neq k,j,m} \left[f_{ik} \frac{\partial F\left(x_{ki}\right)}{\partial x_{ki}} \nabla_m f_{mk} + f_{ij} \frac{\partial F\left(x_{ji}\right)}{\partial x_{ji}} \nabla_m f_{mj} \right],
\end{aligned}
\tag{B.6}
$$

Table B.2: Partial derivative values for the cubic spline interpolation of the function $F_{ij}\left(N_i^{(t)}, N_j^{(t)}, N_{ij}^{\text{conj}}\right)$. $F(i, j, k) = F(j, i, k)$, $F(i, j, k > 2) = F(i, j, 2)$, and $\frac{\partial F(i,j,k)}{\partial i} = \frac{\partial F(j,i,k)}{\partial i}$. All partial derivative values not given are zero [82, 116].

	1$^{\text{st}}$ parametrization	2$^{\text{nd}}$ parametrization
$F(2, 3, 1)$, $F(2, 3, 2)$	-0.0465	-0.0363
$F(1, 2, 2)$	-0.0355	-0.0243
$F(1, 1, 1)$	0.1511	0.1264
$F(2, 2, 1)$	0.075	0.0605
$F(1, 2, 1)$	0.0126	0.0120
$F(1, 3, 1)$, $F(1, 3, 2)$	-0.1130	-0.0903
$F(0, 3, 1)$, $F(0, 3, 2)$	-0.1220	-0.0904
$F(0, 2, 2)$	-0.0445	-0.0269
$F(0, 2, 1)$	0.0320	0.0427
$F(0, 1, 1)$	0.1100	0.0996
$F(1, 1, 2)$	0.0074	0.0108
$\frac{\partial F(2,0,1)}{\partial i}$	-0.1160	-0.09950
$\frac{\partial F(2,1,1)}{\partial i}$	-0.13205	-0.10835
$\frac{\partial F(2,0,2)}{\partial i}$	-0.0610	-0.0452
$\frac{\partial F(1,2,2)}{\partial i}$	0.02225	0.01345
$\frac{\partial F(1,3,2)}{\partial i}$	0.03775	-0.02705
$\frac{\partial F(2,3,2)}{\partial i}$	0.0565	0.04515
$\frac{\partial F(2,3,1)}{\partial i}$	0.0565	0.04515
$\frac{\partial F(2,1,2)}{\partial i}$	-0.0602	-0.08760

where again the shorthand notations for $f_{ij}\left(r_{ij}\right)$ and $F_{ij}\left(N_i^{(t)}, N_j^{(t)}, N_{ij}^{\text{conj}}\right)$ have been used. The derivative of $F(x_{ik})$ with respect to x_{ik} is

$$\frac{\partial F(x_{ik})}{\partial x_{ik}} = \begin{cases} 0, & \text{if } x_{ik} \leq 2 \\ -\frac{\pi}{2} \sin[\pi (x_{ik} - 2)], & \text{if } 2 < x_{ik} < 3 \\ 0, & \text{if } x_{ik} \geq 3. \end{cases} \tag{B.7}$$

Equations (3.17), (3.19), and (3.20) have been used to calculate the values of the partial derivatives of Equation (B.5) except for the values of the function F_{ij} and its partial derivatives which are interpolated using a tricubic spline interpolation from the values of Table B.2 [115].

There still remains the cut-off function of Equation (3.13) to differentiate. The gradi-

ent of the cut-off function is

$$\nabla_m f_{mj}\left(r_{mj}\right) = \begin{cases} 0, & \text{if } r_{mj} < R_{mj}^{(1)} \\ -\frac{1}{2}\frac{\pi}{R_{mj}^{(2)}-R_{mj}^{(1)}}\sin\left(\frac{\pi\left(r_{mj}-R_{mj}^{(1)}\right)}{R_{mj}^{(2)}-R_{mj}^{(1)}}\right)\frac{\vec{r}_{mj}}{|r_{mj}|}, & \text{if } R_{mj}^{(1)} < r_{mj} < R_{mj}^{(2)} \\ 0, & \text{if } r_{mj} < R_{mj}^{(2)} \end{cases}$$

$$\nabla_m f_{im}\left(r_{im}\right) = \begin{cases} 0, & \text{if } r_{im} < R_{im}^{(1)} \\ +\frac{1}{2}\frac{\pi}{R_{im}^{(2)}-R_{im}^{(1)}}\sin\left(\frac{\pi\left(r_{im}-R_{im}^{(1)}\right)}{R_{im}^{(2)}-R_{im}^{(1)}}\right)\frac{\vec{r}_{im}}{|r_{im}|}, & \text{if } R_{im}^{(1)} < r_{im} < R_{im}^{(2)} \\ 0, & \text{if } r_{im} < R_{im}^{(2)}, \end{cases}$$

$$(B.8)$$

and zero for all pairs of indices that do not include m.

Now all the terms to compute the acceleration of a particle according to Equation (B.1) have been defined. The time development of the system can be calculated as discussed in Section 3.2.1.

References

[1] H. W. Kroto, J. R. Heath, S. C. O'Brien, R. F. Curl, and R. E. Smalley, Nature **318**, 162 (1985).

[2] S. Iijima, Nature **354**, 56 (1991).

[3] S. Iijima, Nature **363**, 603 (1993).

[4] D. S. Bethune, C. H. Kiang, M. S. de Vries, G. Gorman, R. Savoy, J. Vasquez, and R. Beyers, Nature **363**, 605 (1993).

[5] R. Saito, G. Dresselhaus, and M. S. Dresselhaus, *Physical Properties of Carbon Nanotubes* (Imperial College Press, UK, 1992).

[6] M. S. Dresselhaus, G. Dresselhaus, and P. Avouris (Eds), *Carbon Nanotubes, Synthesis, Structure, Properties and Applications* (Springer, Berlin, 2001).

[7] A. Javey, H. Kim, M. Brink, Q. Wang, A. Ural, J. Guo, P. McIntyre, P. McEuen, M. Lundstrom, and H. Dai, Nature Materials **1**, 241 (2002).

[8] D. R. Lide (Ed.), *CRC Handbook of Chemistry and Physics, 75th Edition* (CRC Press, Inc., USA, 1994).

[9] H. W. Zhu, C. L. Xu, D. H. Wu, B. Q. Wei, R. Vajtai, and P. M. Ajayan, Science **296**, 884 (2002).

[10] L. X. Zheng, M. J. O'Connell, S. K. Doorn, X. Z. Lia, Y. H. Zhao, E. A. Akhadov, M. A. Hoffbauer, B. J. Roop, Q. X. Jia, R. C. Dye, D. E. Peterson, S. M. Huang, J. Liu, and Y. T. Zhu, Nature Materials **3**, 673 (2004).

[11] Z. F. Ren, Z. P. Huang, D. Z. Wang, J. G. Wen, J. W. Xu, J. H. Wang, L. E. Calvet, J. Chen, J. F. Klemic, and M. A. Reed, Appl. Phys. Lett. **75**, 1086 (1999).

[12] H. Kind, J. M. Bonard, L. Forró, K. Kern, K. Hernadi, L. O. Nilsson, and L. Schlapbach, Langmuir **16**, 6877 (2000).

[13] S. Amelinckx, X. B. Zhang, D. Bernaerts, X. F. Zhang, V. Ivanov, and J. B. Nagy, Science **265**, 635 (1994).

[14] L. P. Biró, S. D. Lazarescu, P. A. Thiry, A. Fonseca, J. B. Nagy, A. A. Lucas, and P. Lambin, Europhysics Lett. **50**, 494 (2000).

[15] J. Liu, H. Dai, J. H. Hafner, D. T. Colbert, R. E. Smalley, S. J. Tans, and C. Dekker, Nature **385**, 780 (1997).

[16] R. Martel, H. R. Shea, and P. Avouris, Nature **398**, 299 (1999).

[17] M. Ahlskog, E. Seynaeve, R. J. M. Vullers, C. V. Haesendonck, A. Fonseca, K. Hernadi, and J. B. Nagy, Chem. Phys. Lett. **300**, 202 (1999).

[18] M. Sano, A. Kamino, J. Okamura, and S. Shinkai, Science **293**, 1299 (2001).

[19] M. Ahlskog, C. Laurent, M. Baxendale, and M. Huhtala, Electronic properties and applications of carbon nanotubes, in *Encyclopedia of Nanoscience and Nanotechnology*, edited by H. S. Nalwa Vol. 3, p. 139, American Scientific Publishers, USA, 2004.

[20] L. Chico, L. X. Benedict, S. G. Louie, and M. L. Cohen, Phys. Rev. B **54**, 2600 (1996).

[21] L. Chico, V. H. Crespi, L. X. Benedict, S. G. Louie, and M. L. Cohen, Phys. Rev. Lett. **76**, 971 (1996).

[22] M. Bockrath, W. Liang, D. Bozovic, J. H. Hafner, C. M. Lieber, M. Tinkham, and H. Park, Science **291**, 283 (2001).

[23] D. Orlikowski, M. B. Nardelli, J. Bernholc, and C. Roland, Phys. Rev. B **61**, 14194 (2000).

[24] M. B. Nardelli and J. Bernholc, Phys. Rev. B **60**, 16338 (1999).

[25] A. Rochefort, D. R. Salahub, and P. Avouris, Chem. Phys. Lett. **297**, 45 (1998).

[26] T. W. Tombler, Chongwu-Zhou, L. Alexseyev, Jing-Kong, Hongjie-Dai, Lei-Liu, C. S. Jayanthi, Meijie-Tang, and Shi-Yu-Wu, Nature (London) **405**, 769 (2000).

[27] A. Maiti, A. Svizhenko, and M. P. Anantram, Phys. Rev. Lett. **88**, 126805 (2002).

[28] H. W. Postma, T. Teepen, Z. Yao, M. Grifoni, and C. Dekker, Science **293**, 76 (2001).

[29] D. Bozovic, M. Bockrath, J. H. Hafner, C. M. Lieber, H. Park, and M. Tinkham, Appl. Phys. Lett. **78**, 3693 (2001).

[30] K. Ishibashi, D. Tsuya, M. Suzuki, and Y. Aoyagi, Appl. Phys. Lett. **82**, 3307 (2003).

[31] P. G. Collins, M. S. Arnold, and P. Avouris, Science **292**, 706 (2001).

[32] M. M. J. Treacy, T. W. Ebbesen, and J. M. Gibson, Nature **381**, 678 (1996).

[33] E. W. Wong, P. E. Sheehan, and C. M. Lieber, Science **277**, 1971 (1997).

[34] P. Poncharal, Z. L. Wang, , D. Ugarte, and W. A. de Heer, Science **283**, 1513 (1999).

[35] A. Krishnan, E. Dujardin, T. W. Ebbesen, P. N. Yianilos, and M. M. J. Treacy, Phys. Rev. B **58**, 14013 (1998).

[36] E. Hernández, C. Goze, P. Bernier, and A. Rubio, Phys. Rev. Lett. **80**, 4502 (1998).

[37] J. P. Lu, Phys. Rev. Lett. **79**, 1297 (1997).

[38] M.-F. Yu, O. Lourie, M. J. Dyer, K. Moloni, T. F. Kelly, and R. S. Ruoff, Science **287**, 637 (2000).

[39] F. Li, H. M. Cheng, S. Bai, G. Su, and M. S. Dresselhaus, Appl Phys. Lett. **77**, 3161 (2000).

[40] M.-F. Yu, B. S. Files, S. Arepalli, and R. S. Ruoff, Phys. Rev. Lett. **84**, 5552 (2000).

[41] D. A. Walters, L. M. Ericson, M. J. Casavant, J. liu, D. T. Colbert, K. A. Smith, and R. E. Smalley, Appl. Phys. Lett. **74**, 3803 (1999).

[42] C. Wei, K. Cho, and D. Srivastava, Appl. Phys. Lett. **82**, 2512 (2003).

[43] T. Belytschko, S. P. Xiao, G. C. Schatz, and R. S. Ruoff, Phys. Rev. B **65**, 235430 (2002).

[44] B. I. Yakobson, M. P. Campbell, C. J. Brabec, and J. Bernholc, Comp. Mat. Sci. **8**, 341 (1997).

[45] C. Wei, K. Cho, and D. Srivastava, Phys. Rev. B **67**, 115407 (2003).

[46] B. I. Yakobson, C. J. Brabec, and J. Bernholc, Phys. Rev. B **76**, 2511 (1996).

[47] B. I. Yakobson, M. P. Campbell, C. J. Brabec, and J. Bernholc, Comput. Mat. Sci. **8**, 341 (1997).

[48] M. R. Falvo, G. J. Clary, R. M. Taylor, V. Chi, F. P. Brooks, S. Washburn, and R. Superfine, Nature **389**, 582 (1997).

[49] M. B. Nardelli, B. I. Yakobson, and J. Bernholc, Phys. Rev. B **57**, 4277 (1998).

[50] M. B. Nardelli, B. I. Yakobson, and J. Bernholc, Phys. Rev. Lett. **81**, 4656 (1998).

[51] Q. Zhao, M. B. Nardelli, and J. Bernholc, Phys. Rev. B **65**, 144105 (2002).

[52] A. B. Dalton, S. Collins, E. Munoz, J. M. Razal, V. H. Ebron, J. P. Ferraris, J. N. Coleman, B. G. Kim, and R. H. Baughman, Nature (London) **703**, 423 (2003).

[53] M. Cadek, J. N. Coleman, V. Barron, K. Hedicke, and W. J. Blau, Appl. Phys. Lett. **81**, 5123 (2002).

[54] A. H. Barber, S. R. Cohen, and H. D. Wagner, Appl. Phys. Lett. **82**, 4140 (2003).

[55] J. Cummings and A. Zettl, Science **289**, 602 (2000).

[56] M. Yu, B. I. Yakobson, and R. S. Ruoff, J. Phys. Chem. B **104**, 8764 (2000).

[57] S. Akita and Y. Nakayama, Jpn. J. Appl. Phys. **42**, 3933 (2003).

[58] S. Akita and Y. Nakayama, Jpn. J. Appl. Phys. **42**, 4830 (2003).

[59] A. N. Kolmogorov and V. H. Crespi, Phys. Rev. Lett. **85**, 4727 (2000).

[60] S. B. Legoas, V. R. Coluci, S. F. Braga, P. Z. Coura, S. O. Dantas, and D. S. G. ao, Phys. Rev. Lett. **90**, 55504 (2003).

[61] Q. Zheng and Q. Jiang, Phys. Rev. Lett. **88**, 45503 (2002).

[62] Q. Zheng, J. Z. Liu, and Q. Jiang, Phys. Rev. B **65**, 245409 (2002).

[63] W. Guo, Y. Guo, H. Gao, Q. Zheng, and W. Zhong, Phys. Rev. Lett. **91**, 125501 (2003).

[64] A. M. Fennimore, T. D. Yuzvinsky, W.-Q. Han, M. S. Fuhrer, J. Cumings, and A. Zettl, Nature (London) **424**, 408 (2003).

[65] G. Zhang, X. Jiang, and E. Wang, Science **300**, 472 (2003).

[66] F. Banhart, Rep. Prog. Phys. **62**, 1181 (1999).

[67] A. V. Krasheninnikov and K. Nordlund, Nucl. Instr. and Meth. in Phys. Res. B **216**, 355 (2004).

[68] A. V. Krasheninnikov, K. Nordlund, M. Sirviö, E. Salonen, and J. Keinonen, Phys. Rev. B **63**, 245405 (2001).

[69] A. V. Krasheninnikov, K. Nordlund, and J. Keinonen, Phys. Rev. B **65**, 165423 (2002).

[70] C.-H. Kiang, W. A. Goddard, R. Beyers, and D. S. Bethune, J. Phys. Chem. **100**, 3749 (1996).

[71] M. Terrones, H. Terrones, F. Banhart, J.-C. Charlier, and P. M. Ajayan, Science **288**, 1226 (2000).

[72] M. Terrones, F. Banhart, N. Grobert, J.-C. Charlier, H. Terrones, and P. Ajayan, Phys. Rev. Lett. **89**, 075505 (2002).

[73] P. M. Ajayan, V. Ravikumar, and J.-C. Charlier, Phys. Rev. Lett. **81**, 1437 (1998).

[74] M. Suzuki, K. Ishibashi, K. Toratani, D. Tsuya, and Y. Aoyagi, Appl. Phys. Lett. **81**, 2273 (2002).

[75] H. Stahl, J. Appenzeller, R.Martel, P. Avouris, and B. Lengeler, Phys. Rev. Lett. **85**, 5186 (2000).

[76] B. Ni, R. Andrews, D. Jacques, D. Qian, M. B. J. Wijesundara, Y. Choi, L. Hanley, and S. B. Sinnott, Applied. Physics A: Mater. Sci. Process. **105**, 12719 (2001).

[77] A. V. Krasheninnikov, K. Nordlund, and J. Keinonen, Appl. Phys. Lett. **81**, 1101 (2002).

[78] E. Salonen, A. V. Krasheninnikov, and K. Nordlund, Nucl. Instr. and Meth. in Phys. Res. B **193**, 603 (2002).

[79] A. Kis, G. Csányi, J.-P. Salvetat, T.-N. Lee, E. Couteau, A. J. Kulik, W. Benoit, J. Brugger, and L. Forró, Nature Materials **3**, 153 (2004).

[80] R. Telling, C. Ewels, A. El-Barbary, and M. Heggie, Nature Materials **2**, 333 (2003).

[81] B. Ni and S. B. Sinnott, Phys. Rev. B **61**, 16343 (2000).

[82] D. W. Brenner, Phys. Rev. B **42**, 9458 (1990).

[83] S. J. Stuart, A. B. Tutein, and J. A. Harrison, J. Chem. Phys. **112**, 6472 (2000).

[84] T. Frauenheim, G. Seifert, M. Elstner, T. Niehaus, C. Köhler, M. Amkreutz, M. Sternberg, Z. Hajnal, A. Di Carlo, and S. Suhai, J. Phys.: Condens. Matter **14**, 3015 (2002).

[85] M. Elstner, D. Porezag, G. Jungnickel, J. Elsner, M. Haugk, T. Frauenheim, S. Suhai, and G. Seifert, Phys. Rev. B **58**, 7260 (1998).

[86] N. W. Ascroft and N. D. Mermin, *Solid State Physics* (Saunders, USA, 1976).

[87] P. Hohenberg and W. Kohn, Phys. Rev. **136**, B864 (1964).

[88] W. Kohn and L. J. Sham, Phys. Rev. **140**, A1133 (1965).

[89] C. J. Cramer, *Essentials of Computational Chemistry* (John Wiley & Sons, Inc., USA, 2002).

[90] C. M. Goringe, D. R. Bowler, and E. Hernández, Rep. Prog. Phys. **60**, 1447 (1997).

[91] D. C. Rapaport, *The Art of Molecular Dynamics Simulation* (Cambridge University Press, UK, 1995).

[92] M. P. Allen and D. J. Tildesley, *Computer Simulation of Liquids* (Clarendon, UK, 1987).

[93] J. Tersoff, Phys. Rev. Lett. **56**, 632 (1986).

[94] J. Tersoff, Phys. Rev. B **27**, 6991 (1988).

[95] J. Tersoff, Phys. Rev. B **39**, 5566 (1989).

[96] N. Metropolis, A. W. Rosenbluth, M. N. Rosenbluth, A. H. Teller, and E. Teller, J. Chem. Phys. **21**, 1087 (1953).

[97] C. W. Gear, *Report ANL 7126: The numerical integration of ordinary differential equations of various orders* (Argonne National Laboratory, USA, 1966).

[98] C. W. Gear, *Numerical initial value problems in ordinary differential equations.* (Prentice-Hall, NJ, USA, 1971).

[99] R. K. Pathria, *Statistical Mechanics, 2nd edition* (Butterworth Heinemann, USA, 1996).

[100] G. C. Abell, Phys. Rev. B **31**, 6184 (1985).

[101] H. U. Jäger and K. Albe, J. Appl. Phys. **88**, 1129 (2000).

[102] V. Meunier, M. B. Nardelli, C. Roland, and J. Bernholc, Phys. Rev. B **64**, 195419 (2001).

[103] J. Bernholc, C. Brabec, M. B. Nardelli, A. Maiti, C. Roland, and B. I. Yakobson, Appl. Phys. A. **67**, 39 (1998).

[104] K. Nordlund, J. Keinonen, and T. Mattila, Phys. Rev. Lett. **77**, 699 (1996).

[105] H. R. Shea, R. Martel, and P. Avouris, Phys. Rev. Lett. **84**, 4441 (2000).

[106] L. Liu, G. Y. Guo, C. S. Jayanthi, and S. Y. Yu, Phys. Rev. Lett. **88**, 217206 (2002).

[107] G. Cuniperti, J. Yi, and M. Porto, Appl. Phys. Lett. **81**, 850 (2000).

[108] S. Latil, S. Roche, and A. Rubio, Phys. Rev. B **67**, 165420 (2003).

[109] O. Lourie, D. M. Cox, and H. D. Wagner, Phys. Rev. Lett. **81**, 1638 (1998).

[110] A. Maiti, Chem. Phys. Lett. **331**, 21 (2000).

[111] J. Seldin and C. W. Nezbeda, J. Appl. Phys. **41**, 3389 (1970).

[112] J. P. Salvetat, J. M. Bonard, N. H. Thomson, A. J. Kulik, L. Forró, W. Benoit, and L. Zuppiroli, Applied-Physics-A-(Materials-Science-Processing) **69**, 255 (1999).

[113] B. W. Smith and D. E. Luzzi, J. Appl. Phys. **90**, 3509 (2001).

[114] F. W. Byron and R. W. Fuller, *Mathematics of classical and quantum physics* (Dover Publications, Inc., USA, 1992).

[115] K. Beardmore and R. Smith, Phil. Mag. A **74**, 1439 (1996).

[116] D. W. Brenner, Phys. Rev. B **46**, 1948 (1992).